Research Square

Preprints are preliminary reports that have not undergone peer review.
They should not be considered conclusive, used to inform clinical practice,
or referenced by the media as validated information.

MMP3-PKM2 axis controls loading of the glycolytic system in extracellular vesicles and macrophage polarity in oral cancer

Takanori Eguchi

p81v6907@s.okayama-u.ac.jp

Okayama University https://orcid.org/0000-0002-3297-6126

Eman Taha

Ain Shams University

Kunihiro Yoshida

Okayama University

Htoo Shwe Eain

Okayama University

Hiroki Shinchi

Japanese Foundation for Cancer Research

Yichun Wang

Okayama University

Lizi Xing

The University of Auckland

Mona Sheta

Cairo University

May Wathone Oo

Miyazaki University

Hotaka Kawai

Okayama University

Kuniaki Okamoto

Okayama University

Koji Ueda

Japanese Foundation for Cancer Research https://orcid.org/0000-0001-9066-4959

Article

Keywords: Extracellular vesicles, head and neck cancer, oral squamous cell carcinoma, proteomics, glycolysis, pyruvate kinase M (PKM), shikonin.

Posted Date: November 3rd, 2026

DOI: https://doi.org/10.21203/rs.3.rs-11314663/v1

License: This work is licensed under a Creative Commons Attribution 4.0 International License.
Read Full License

Additional Declarations: There is no conflict of interest

Abstract

Extracellular vesicles (EVs) mediate intercellular communication and microenvironmental remodeling in oral squamous cell carcinoma (OSCC). Our proteomic analysis revealed that OSCC EVs contain the complete suite of anaerobic glycolytic enzymes, with pyruvate kinase M2 (PKM2) and GAPDH significantly enriched. Moreover, matrix metalloproteinase-3 (MMP-3) regulated EV secretion and glycolytic cargo loading. MMP3 knockout in tumoroids markedly reduced EV release and impaired the loading of glycolytic enzymes, including PKM2. Co-culture assays showed that cancer EVs transfer PKM2 and MMP3 to recipient macrophages in an MMP3-dependent manner. EV subtypes exerted distinct effects on macrophage polarity: MMP3-loaded large EVs (LEVs) selectively induced immunosuppressive M2 macrophage polarization (elevated MRC1, decreased NOS2), whereas MMP3-loaded small EVs (SEVs) modulated both M1 and M2 phenotypes. Clinical database analysis confirmed that high PKM expression correlates with poor overall survival in head and neck cancer. Pharmacological PKM2 inhibition with shikonin suppressed EV release in a concentration-dependent manner and reduced OSCC cell viability in 2D and 3D cultures. Together, the MMP3–PKM2 axis controls EV glycolytic cargo loading and dictates subtype-dependent macrophage polarization.

Introduction

Head and neck squamous cell carcinoma (HNSC) ranks as the seventh most common malignancy worldwide, with approximately 890,000 new cases and 450,000 deaths annually, accounting for 4.5% of global cancer diagnoses and fatalities [1]. Oral squamous cell carcinoma (OSCC) is the most prevalent form of head and neck cancer and represents approximately 90% of all cases [2]. OSCC alone contributes to 3% of global malignancies and is the 17th leading cause of cancer-related mortality [3, 4]. OSCC lesions are usually found in the tongue, alveolar ridge, gingiva, floor of the mouth, buccal mucosa, and palate. Despite recent advancements in many therapeutic strategies, HNSC remains associated with recurrence and progression. More than 50% of HNSC patients exhibit lymph node (LN) metastasis, a major adverse prognostic factor [4, 5]. The 5-year survival rate of primary HNSC patients is greater than 80%, but it falls to 40% with cervical LN metastasis and to 20% with distant metastases [6]. Cancer progression is often associated with extracellular molecules released by cancer cells into the milieu [7]. Such secreted molecules can educate cells in autocrine, paracrine, and/or endocrine manners, thereby inducing changes in tumor, stromal, endothelial, immune/inflammatory, and distant cells [8].

Extracellular vesicles (EVs) are small extracellular particles surrounded by lipid bilayers, ranging in diameter from 30 nm to 20 μm, secreted by cells [9, 10]. EVs carry cell-derived cargo molecules, such as proteins, nucleic acids, lipids, and metabolites, either inside or on their surface. EVs carrying cargo molecules are found in body fluids, such as blood, saliva and urine, as well as in cell/tissue culture supernatants. EVs are often surrounded by a protein corona, including apolipoproteins and immunoglobulins, which are initially derived from body fluids such as blood plasma or serum [11, 12]. EV cargo molecules have been developed as prognostic biomarkers of diseases, including cancers, and as indicators of pathophysiological body status. Notably, EV-mediated intercellular molecular transfer is

essential for intercellular communication and recipient cell fate [13, 14]. Through molecular transfer, cancer cell-derived EVs largely organize tumor-associated cells in the tumor microenvironment (TME) and distant cells to form a metastatic niche [8, 15, 16]. Our previous study showed that LN-metastatic oral cancer EVs induce epithelial-to-mesenchymal transition (EMT), promote cancer cell migration and invasion, enhance stem-like traits, and polarize tumor-associated macrophages (TAMs) toward tumor-supporting M2-type macrophages [17, 18]. In the present study, we show that pyruvate kinase M2 (PKM2) and matrix metalloproteinase 3 (MMP-3), which are abundant in cancer EVs, regulate TAM polarization.

The glycolytic phenotype is a hallmark of most cancers [19]. A near-universal property of primary and metastatic cancers is upregulated glycolysis, which increases glucose consumption. Clinical tumor imaging commonly shows increased glucose uptake. Glycolytic upregulation results from active selection processes and must confer a significant, identifiable growth advantage. Constitutive upregulation of glycolysis is likely an adaptation to hypoxia that develops as premalignant lesions grow progressively farther from their blood supply [19]. Warburg's hypothesis for cancer progression is that cancer cells undergo a two-step transformation. First, mitochondrial respiration fails irreversibly, and second, the cell survives by anaerobic glycolytic fermentation for energy. Anaerobic glycolytic fermentation is far less efficient than mitochondrial aerobic glycolysis, producing only 2 ATP per glucose molecule as opposed to 38 via mitochondrial aerobic glycolysis [20]. Pyruvate kinase M2 (PKM2) is a key rate-limiting enzyme in anaerobic glycolysis that catalyzes the final step and is associated with tumor metabolism and growth [21, 22]. In cancer cells, PKM2 expression is upregulated, whereas tissue-specific PKM1, derived from a single PKM gene through alternative splicing of a primary mRNA transcript, declines [23]. Past research shows that PKM2 is involved in both glycolytic and non-glycolytic pathways and is instrumental in tumor cell malignancy through its metabolic and non-metabolic functions [22, 24]. PKM2 plays a dual role in regulating glycolysis and nuclear translocation, thereby activating the cyclin D1 (CCND1) gene and driving the cell cycle in HNSC [25]. In the present study, we found that oral cancer EVs harbor all anaerobic glycolytic enzymes, including PKM. High PKM expression was associated with poor prognosis in many cancer types. Notably, PKM2 promoted EV secretion and cell viability in oral cancer.

Matrix metalloproteinases (MMPs) are a family of zinc-dependent proteinases that belong to the group of endopeptidases or matrixins [26], and also act as transcription factors [27–29]. They can cleave a wide range of substrates, including extracellular matrix (ECM) components and cell-surface-associated proteins, as well as intracellular targets [30]. Accordingly, MMPs play key roles in various physiological and pathological processes, including tissue homeostasis and cancer cell invasion within the TME [30–32]. Notably, MMP-3 has been shown to promote EV integrity and EV-driven tumor growth in cancer [33, 34]. However, it remains unexplored whether MMP-3 controls EV secretion and glycolytic enzymes. In the present study, we found that the MMP3-PKM2 axis is essential for EV glycolytic system secretion and macrophage polarization in the TME.

Results

The MMP3-PKM axis is essential for extracellular vesicle glycolytic system secretion.

To identify the proteome of oral cancer EVs, we isolated EVs from oral cancer cells (SAS, HSC-2, HSC-3, and M3) using the FC-AP and FC-P methods and analyzed them using mass spectrometry. We identified 5264 and 4572 protein types using the FC-AP and FC-P methods, respectively (Fig. 1A). Surprisingly, all anaerobic glycolytic enzymes were contained in oral cancer EVs, including hexokinase (HK1/2), glucose-6-phosphate isomerase (GPI), phosphofructokinase-1 (PFKM), aldolase (ALDO-A/B/C), glyceraldehyde-3-phosphate dehydrogenase (GAPDH), phosphoglycerate kinase (PGK), phosphoglyceromutase (PGAM 1/2), enolase (ENO1), pyruvate kinase liver-type/red blood cell-type (PKLR), and pyruvate kinase muscle-type (PKM), on par with Category 1 EV markers such as CD9 and Alix (Fig. 1B, C; Figure S1).

Tumoroids generated in 3D culture systems have characteristics similar to those of in vivo tumors, including hypoxia, intercellular adhesion, slow proliferation and metabolism, and drug resistance [16, 35, 36]. We performed EV multi-omics, including transcriptomes and proteomes, comparing LuM1^{MMP3high} and MMP3-knockout (KO) tumoroid-derived EVs (Fig. 2A, Figure S2). Bubble plot analysis of RNA-seq data revealed marked alterations in the metabolic pathway (75 genes), the focal adhesion pathway, and the tight junction pathway following MMP3 KO (Fig. 2B). Several glycolytic enzyme transcripts (*Aloa, Pkm, Eno1*, and *Ldha*) were highly expressed in EVs (Fig. 2C), while MMP3 KO reduced multiple glycolytic enzyme transcripts in EVs, including *Hk1, Pfkp, Pfkl, Pfkm*, and *Aldoa* (Fig. 2D). Additionally, MMP3 KO significantly reduced EV secretion by tumoroids (Fig. 2E). Proteomic analysis further demonstrated that MMP3, PKM and GAPDH were abundant in LuM1-EVs but were markedly reduced in MMP3KO-EVs (Fig. 2F–I). In contrast, other glycolytic enzymes, including PGK1 and ENO1, remained abundant in both LuM1-EVs and MMP3KO-EVs (Fig. 2J, K). These findings suggest that the MMP3–PKM axis regulates glycolytic cargo loading into extracellular vesicles in oral cancer.

EV-mediated transfer of PKM2 and MMP3 from cancer cells to macrophages.

A recent study demonstrated that ectosomal (large EV) PKM2 promotes hepatocellular carcinoma (HCC) progression by inducing macrophage differentiation and remodeling within the TME [37]. ERK-1/2-dependent phosphorylation and nuclear translocation of PKM2 promote the Warburg effect [38]. To test whether cancer cells transfer PKM2 and MMP3 to macrophages, we established direct and indirect co-culture systems using macrophages and cancer cells (Fig. 3A, Figure S3A). Both direct and indirect co-cultures (pore size: 0.1, 0.4 or 1.0 μm) of cancer cells (M3) induced the M2-type macrophage marker MRC1 expression, suggesting that cancer-derived SEVs and LEVs induce M2-type macrophage polarity (Figure S3B). In the indirect culture system with a 0.1 μm pore size, membrane-bound pTomato expressed in LuM1 cells was detected in recipient macrophages and colocalized with the M2 macrophage marker MRC1, suggesting that pTomato was transferred via small EVs (Fig. 3B, Figure S3C). Confocal microscopy showed that nuclear phosphorylated PKM2 (pPKM2) was detected in MRC1-positive and MMP3-positive macrophages in the indirect co-culture using 1.0 μm pore inserts (Fig. 3C). qICC showed that the pPKM2-positive macrophage rate, pPKM2-positive area/cell, and pPKM2 expression/cell increased significantly under both direct and indirect co-culture with LuM1 cells. In

contrast, MMP3 knockout attenuated PKM2 transfer from cancer cells to macrophages, indicating that PKM2 transfer is dependent on MMP3 (Fig. 3D–J). Similarly, MMP3-positive macrophage frequency, area/cell, and expression/cell were increased in both direct and indirect co-cultures with LuM1 cells. However, MMP3 knockout reduced MMP3 transfer under direct co-culture and the 0.1-μm indirect co-culture (Fig. 3K–Q). Exceptionally, MMP3-positive cell rate, area/cell, and expression/cell in macrophages were comparable between LuM1 and MMP3 cells under 1.0-μm co-culture conditions, indicating that cancer-derived large EVs may induce endogenous MMP3 expression in macrophages (Fig. 3O–Q).

Overall, these data indicate that cancer EVs transfer PKM2 and MMP3 to macrophages, and that MMP3 is required for efficient EV-mediated PKM2 transfer.

Cancer-derived large and small EVs polarize macrophages.

We next isolated LEVs and SEVs from RT7 (normal oral epithelial cell line), M3 (metastatic oral cancer cell line), and M3pToma cells, which secrete red-fluorescent EVs, and analyzed them using TEM, DLS, and FCM (Fig. 4A). Cup-like SEVs sized approximately 100 nm were found in the SEV fraction, whereas LEVs sized approximately 500 nm and migrasome fragments were found in the LEV fraction (Fig. 4B). The size range of SEVs was 70–200 nm in diameter, whereas that of LEVs was 200–1000 nm in diameter (Fig. 4C). In FCM, we detected green autofluorescence in both SEVs and LEVs and pTomato red fluorescence only in M3pToma-EVs but not in M3-EVs, indicating that EVs were successfully labeled with palmtdTomato (Fig. 4D). The red fluorescent LEVs and SEVs were reduced by Triton X-100 treatment, indicating that LEV and SEV membranes were labeled with pTomato and solubilized by Triton X-100 (Figure S4A–C). We next examined whether collecting the supernatant 3 times over 144 hours increased SEV and LEV yields (Figure S4D). SEV and LEV yields were significantly higher in 144-hour, 3-times collection than in 24-hour single collection (Figure S4E, F). The metastatic M3 cells released a higher concentration of LEVs than the normal epithelial RT7 cells, whereas the concentrations of SEVs were not different between these cell lines (Figure S4G).

TAMs are commonly classified as M1-like (pro-inflammatory, inducing anti-tumor immune response) and M2-like (immunosuppressive, promoting tumor progression) phenotypes. We next investigated whether oral cancer LEVs or SEVs modulate macrophage polarity by performing qICC for the M2 marker MRC1 (CD206) and the M1 marker NOS2. Both LEVs and SEVs significantly increased MRC1 expression/cell, MRC1 area/cell, and MRC1-positive cell rate in THP1-derived macrophages (Fig. 4E–H). Conversely, both LEVs and SEVs significantly decreased NOS2 expression/cell, NOS2 area/cell, and NOS2-positive cell rate (Fig. 4I–K). These findings indicate that oral cancer-derived LEVs and SEVs polarize macrophages toward an M2-type and reduce M1-like phenotypes. To investigate whether MMP3-loaded EVs influence macrophage polarization, we examined MRC1 and NOS2 under direct and indirect co-culture conditions. The MRC1-positive cell rate, area/cell, and expression/cell were increased in macrophages co-cultured with LuM1 cells compared to MMP3KO cells (Fig. 5A–G), suggesting that MMP3-loaded large EVs induce M2 polarization. The NOS2 expression was decreased in macrophages under LuM1 direct and

1.0-μm indirect co-cultures compared with MMP3KO (Fig. 5H–N), suggesting suppression of M1-like polarization in the presence of MMP3-loaded large EVs. Exceptionally, the NOS2-positive cell rate, area/cell, and expression/cell in macrophages were increased under direct and indirect (0.1-μm and 0.4-μm) co-cultures, whereas the MMP3 knockout reduced NOS2 expression in macrophages (Fig. 5L–N), suggesting that MMP3-loaded small EVs can induce macrophage M1 polarization. These data suggest that MMP3-loaded small EVs polarize recipient macrophages into both M1 and M2 phenotypes, whereas MMP3-loaded large EVs induce macrophages towards M2 polarization.

Elevated PKM gene expression is associated with poor prognosis in multiple cancer types.

The PKM gene undergoes alternative splicing to produce two major isoforms, PKM1 and PKM2, which exhibit tissue-specific expression patterns [22]. PKM2 includes alternative exon 10 and is commonly expressed in proliferating and tumor tissues, whereas PKM1 includes alternative exon 9 and is predominantly expressed in differentiated tissues such as heart, muscle, and brain [22]. We analyzed databases and found that the PKM gene produces multiple mRNA variants and protein isoforms, including PKM1- and PKM2-related variants, as well as additional protein-coding variants and noncoding RNA transcripts (Figure S5). However, bulk RNA-seq and proteomics datasets, including those used in this study, do not distinguish between specific isoforms.

PKM mRNA was broadly expressed across multiple cancer types, with relatively higher expression in HNSC compared to other cancer types (Fig. 6A, Figure S6). PKM mRNA expression was increased in tumor tissues compared with paired normal tissues across multiple cancer types, including HNSC, colon adenocarcinoma (COAD), rectum adenocarcinoma (READ), breast carcinoma (BRCA), cervical squamous cell carcinoma (CESC), cholangiocarcinoma (CHOL), diffuse large B-cell lymphoma (DLBC), kidney renal clear cell carcinoma (KIRC), kidney renal papillary cell carcinoma (KIRP), lung squamous cell carcinoma (LUSC), ovarian cancer (OV), pancreatic adenocarcinoma (PAAD), skin cutaneous melanoma (SKCM), stomach adenocarcinoma (STAD), uterine corpus endometrial carcinoma (UCEC), and uterine carcinosarcoma (UCS) (Fig. 6B).

High PKM expression in HNSC was associated with poor patient survival (HR = 1.65, p = 0.00049) especially at stage IV (HR = 2.02, p = 0.00023) (Fig. 6C–E), in CESC (HR = 2.05, p = 0.0086), hepatocellular carcinoma (HCC) (HR = 2.23, p = 7.2 × 10^-6), lung adenocarcinoma (HR = 1.72, p = 0.00026), OV (HR = 1.39, p = 0.022), PAAD (HR = 2.46, p = 1.8 × 10^-5), and thymoma (HR = 3.94, p = 0.038) (Fig. 6F–H, Figure S6D–F).

These findings suggest that elevated PKM expression is associated with poor prognosis in different types of cancer.

Expression of total PKM and phosphorylated PKM2 in oral carcinomas.

scRNA-seq analysis of primary tumors from patients with HNSC identified distinct malignant, stromal, immune, and other cell populations (Fig. 7A). PKM mRNA was widely expressed in these cell

populations, with prominent expression in malignant cells, monocytes, fibroblasts, macrophages and endothelial cells, while expression was relatively low in B cells/plasma cells and dendritic cells (Fig. 7B).

PKM gene has two mRNA variants, PKM1 and PKM2; PKM2 is commonly expressed in proliferating and tumor tissues, whereas PKM1 is predominantly expressed in differentiated cells [22]. ERK-1/2-dependent phosphorylation and nuclear translocation of PKM2 promote the Warburg effect [38]. To examine pPKM2 expression and M2-type macrophage presence across oral carcinoma types, we generated immunogenic and immunosuppressive tumors in orthotopic mouse models and performed IHC for M2 markers (CD206 and CD163) and pPKM2. As expected, the numbers of CD206-positive macrophages and CD163-positive macrophages were significantly higher in the immunosuppressive tumors (MOC2) than in the immunogenic tumors (MOC1) (Fig. 7C–F). Cells with pPKM2-positive nuclei and cytoplasm were present in both immunogenic and immunosuppressive tumors but were significantly more abundant in immunogenic than in immunosuppressive tumors (Fig. 7G–I, Figure S7).

These data suggest that pPKM2 is abundant in oral carcinoma and contributes to immunogenicity.

PKM2 regulates EV secretion and viability in oral cancer.

Membrane-bound Gaussia luciferase (mbGluc) was used to detect and quantify EV secretion in cell culture supernatants without removing serum-derived non-EV components, including albumin, lipoproteins, and residual bovine EVs. (Fig. 8A,B) [17]. Using this system, we next examined whether pharmacological modulation of PKM2 affects EV secretion in oral cancer cells (M3/mbGluc). Cells were treated with PKM2 inhibitors (shikonin and PKM2-IN-1) or activators (mitapivat and TEPP-46) to assess whether these drugs affect EV secretion in oral cancer cells (M3/mbGluc). Shikonin treatment significantly reduced EV secretion in a concentration-dependent manner (Fig. 8C), suggesting that PKM2 inhibition suppresses EV release. Consistently, PKM2-IN-1 treatment modestly reduced EV secretion at 0.1 and 1 μM (Fig. 8D). In contrast, pharmacological activation of PKM2 using mitapivat or TEPP-46 did not significantly alter EV secretion (Fig. 8E, F). Collectively, these findings suggest that PKM2 activity is associated with EV secretion regulation in oral cancer cells.

In this study, we investigated the association between PKM2-related metabolic activity and tumor cell viability in oral cancer. PKM2 is a key glycolytic enzyme that has also been implicated in transcriptional regulation of genes involved in cell proliferation, including cyclin D1 (CCND1) [25]. Based on these functions, we examined whether pharmacological modulation of PKM2 using inhibitors or activators affects the viability of oral cancer cells (M3 cells). Shikonin significantly reduced oral cancer cell viability in a concentration-dependent manner in both 2D (Fig. 8G–I) and 3D cultures (Fig. 8J–L), despite the drug-resistant phenotype of 3D tumoroids [36]. In contrast, PKM2-IN-1, mitapivat, and TEPP-46 did not significantly affect oral cancer cell viability (Fig. 8M–O, Figure S7). This suggests that shikonin-mediated disruption of PKM2-associated metabolic activity is associated with reduced tumor cell survival. However, the differential effects of PKM2-targeting agents indicate that shikonin may exert broader biological activities beyond PKM2 modulation.

These findings indicate that PKM2 regulates EV release and viability in oral cancer.

Discussion

Our proteomics analyses revealed that oral cancer-derived EVs contain multiple glycolytic enzymes, suggesting that tumor EVs may modulate TME metabolism and that cancer cells maintain intratumoral energy production by EV-mediated transfer of glycolytic pathway enzymes. Among the identified glycolytic enzymes, PKM2 was highly enriched and associated with EV secretion and macrophage polarization. In addition, PKM2 expression was elevated across multiple cancer types and is associated with poor prognosis in several malignancies. Pharmacological inhibition with shikonin reduced EV secretion and oral cancer cell viability, suggesting that PKM2-associated metabolic pathways contribute to tumor progression.

Our data suggest that the transfer of glycolytic system enzymes from metastatic cancer cells to low-metastatic cancer cells could be a novel system for tumors to maintain energy production by the Warburg effect and survival in a low-oxygen tumor microenvironment. Consistently, a recent study reported that a new resistant prostate cancer cell line, PC-3AcT, was resistant to cellular death in an acidic culture medium driven by lactic acid and secreted EVs containing a high abundance of glycolytic enzymes [39]. Moreover, the activation of EV-recipient PC-3 cells can increase glucose consumption and ATP generation, representing an acquired metabolic reprogramming into the Warburg phenotype. Thus, transfer of whole glycolytic system enzymes can be a novel system that largely promotes cancer cell metabolism and survival by maintaining the Warburg effect in a low-oxygen tumor microenvironment.

Our data further suggest that PKM2 may contribute to EV secretion. Consistently, RAB22A has been reported to augment EV secretion by inhibiting PKM2 ubiquitination and degradation [40]. RAB22A also triggers intercellular transmission of chemoresistance in CRC by promoting exosome/EV release via the PKM2-pSNAP23 axis [40]. Moreover, hypoxic microenvironment-induced exosomes/EVs confer temozolomide resistance in glioma by transferring PKM2 [41], further supporting a role for PKM2 in EV-mediated intercellular communication and therapy resistance. Together, these findings support the notion that PKM2-associated EV secretion and transfer contribute to cancer progression and chemoresistance.

Our findings also support the existence of an MMP3-EVs-PKM axis. MMP3 has been reported to maintain EV integrity, promote EV-driven tumor progression, and enhance EV secretion in cancer [29, 32–34]. Moreover, a recent study demonstrated that MMP3 promotesthe secretion of autophagic EVs [30], suggesting that autophagy-related pathways may participate in the MMP3-EV-PKM axis. Autophagosomes can fuse with multivesicular bodies to form amphisomes, which then fuse with the plasma membrane and release cytoplasm-derived cargo with exosomes/sEVs, termed autophagic EVs through exophagy [8, 30]. Alternatively, autophagolysosomes may directly fuse with the plasma membrane to release autophagosomal contents [42]. Although this study did not directly examine these

mechanisms, these recent studies provide plausible pathways through which PKM2-containing EVs may be secreted via exophagy or autophagolysosomal pathways.

Extracellular PKM2 may also contribute to signaling within the TME. Secreted PKM2 has been shown to promote lung cancer metastasis through the integrin β1/FAK signaling pathway [43], suggesting that extracellular or EV-associated PKM2 can directly interact with integrin β1 and influence extracellular matrix-related signaling. Our data also suggest that EV- transferred PKM may enhance glycolytic activity in recipient cells within the TME. In addition, recent studies have also described metabolically active extracellular structures, including extracellular mitochondria [44] and blebbisomes, which are large, cell-like EVs containing mitochondria that take up and release small EVs [10, 45]. Therefore, extracellular PKM may contribute to glycolysis in extracellular compartments such as extracellular mitochondria and blebbisomes, thereby producing energy in the TME.

Our results further show that shikonin inhibits EV secretion and oral cancer cell viability, likely by inhibiting PKM2. Consistently, shikonin has been shown to inhibit ESCC tumor growth by suppressing PKM2-mediated aerobic glycolysis and STAT3 phosphorylation [46]. Shikonin has also been reported to inhibit skin carcinogenesis by reducing cell proliferation [47] and to overcome cisplatin resistance in bladder cancer by inducing necroptosis [48]. Furthermore, shikonin-mediated PKM2 inhibition suppresses TGF-β1 expression by repressing histone lactylation [49], suggesting a link between metabolic regulation and epigenetic control of immunosuppressive signaling. Because TGF-β is a major driver of M2 macrophage polarization, shikonin may modulate immunosuppression in the TME through the PKM2-TGFβ axis.

Our data also suggest that oral cancer-derived EVs transfer PKM2 to recipient cells, including macrophages, thereby contributing to TME immune remodeling. Oral cancer EVs have previously been shown to induce M2 macrophage polarization [17]. Similarly, ectosomal PKM2 promotes HCC progression by driving monocyte-to-macrophage differentiation and remodeling the TME [37]. In this study, sumoylation facilitates ARRDC1-dependent sorting of PKM2 into ectosomes, and ectosomally transferred PKM2 forms a complex with STAT3 and transactivates the macrophage differentiation transcription factors (MafB, c-Maf, and Egr1) [37]. Additionally, macrophage-secreted chemokine CCL1 (M2b marker) reinforced PKM2 ectosomal excretion in a feedforward loop. Collectively, these support the possibility that EV-associated PKM2 contributes to M2-like macrophage polarization through reciprocal signaling mechanisms within the TME.

EVs-PKM2 may also contribute to angiogenesis in the TME. Under hypoxic conditions, PKM2 interacts with NF-κB/p65 and HIF-1α, triggering VEGF-A secretion and subsequent blood vessel formation [50]. This study also showed PKM2 nuclear translocation in pancreatic cancer cells. Based on these findings, EV-derived PKM2 may also translocate into the nuclei of vascular or lymphatic endothelial cells, where PKM2 can activate the HIF1A and VEGF genes.

Finally, the PKM gene encodes multiple variants, including PKM1 and PKM2, as well as additional protein-coding and noncoding RNAs, which complicates precise molecular targeting strategies. PKM1

and PKM2 arise from alternative splicing of exons 9 and 10 and show tissue-specific expression patterns [22]. PKM2, including exon 10, is predominantly expressed in tumors and embryonic tissues, whereas PKM1, including exon 9, is mainly expressed in differentiated tissues such as the heart, muscle, and brain [22]. Consequently, most cancer studies have focused on PKM2. PTBP1-mediated splicing regulation has been shown to promote PKM2 expression, thereby promoting CRC progression [51]. Antisense oligo (ASO)-based splice-switching therapy from PKM2 to PKM1 inhibits HCC growth [52]. In agreement with these reports, our findings show that shikonin-mediated targeting of PKM2 suppresses EV secretion and oral cancer cell viability, supporting PKM2 as a promising therapeutic target. Nevertheless, further studies should also consider additional PKM variants and PKM-independent effects of shikonin. This study has several limitations. Although our findings support the involvement of the MMP3–PKM2–EV axis in oral cancer progression, the precise molecular mechanisms governing EV secretion remain poorly elucidated. In addition, shikonin may exert PKM2-independent effects, and further genetic studies are needed to confirm pathway specificity.

In conclusion, we showed that oral cancer EVs contain the glycolytic system that may contribute to metabolic modulation of the TME and maintain the energy production system in tumors. Among the identified glycolytic enzymes, PKM2 was associated with EV secretion, macrophage polarization, and poor prognosis across multiple cancer types. Pharmacological inhibition of PKM2 using shikonin reduced EV secretion and oral cancer cell viability, supporting a potential role for the PKM2-associated glycolytic system and transcriptional regulation in oral cancer progression.

Materials and Methods

Cell cloning

MMP3-KO LuM1 cells were generated using a CRISPR/Cas9-based genome-editing technology as described previously [34]. Cloning of LuM1 and HSC-3-M3 cells expressing palmitoylation signal-fused (membrane-bound) tandem dimer Tomato (pTomato) was performed as described previously and designated as LuM1pToma and M3pToma, respectively [17, 33]. For luminescent EV labeling, HSC3-M3 (M3) cells were stably transduced with a membrane-bound Gaussia luciferase (mbGluc) reporter. A lentiviral reporter construct, CSCW-*Gaussia* luciferase-biotin acceptor-PDGFRB TM domain-IRES-GFP, was kindly gifted by Dr. Charles P. Lai [53, 54]. For virus production, HEK293T cells at 70–80% confluence were transfected with the construct, psPAX2 packaging plasmid, and pMD2.G envelope plasmid using PEI Max (Polysciences, Warrington, PA, USA). M3 cells were infected using the spinfection method with the viral solution. Infected/transduced stable cells were selected using puromycin. We isolated single clones by limiting dilution to establish M3/mbGluc cell lines.

Cells and tumoroid culture

Human OSCC cell lines (SAS, HSC-2, HSC-3) and a rapidly LN-metastatic subline HSC3-M3 (M3) were obtained from the JCRB Cell Bank. The human normal oral squamous (epithelial) cell line RT7 was kindly provided by Dr. Nobuyuki Kamata (Hiroshima University, Japan). OSCC, M3pToma and M3mbGLuc cells were maintained in DMEM (Wako, Osaka, Japan) supplemented with 10% fetal bovine serum (FBS; Thermo Scientific, Waltham, MA, USA) and a 1% antibiotic-antimycotic solution (Sigma-Aldrich, St. Louis, MO, USA). RT7 cells were cultured in DMEM supplemented with Keratinocyte Growth Medium 2 (KGM2) supplement mix containing recombinant human epidermal growth factor (EGF) (0.125 ng/ml), bovine pituitary extract (0.004 ml/ml), recombinant human insulin (5µg/ml), hydrocortisone (0.33 µg/ml), epinephrine (0.39µg/ml), recombinant human transferrin (10 µg/ml), CaCl2 (0.06 mM), gentamycin and amphotericin B (PromoCell, Heidelberg, Germany). For EV proteomics, OSCC cells were cultured in Essential 8 (E8), a xenofree, serum-free defined medium containing DMEM/F12, bFGF, TGFβ, insulin, transferrin, selenium, and ascorbic acid (Thermo Scientific, Gibco). A rapidly lung-metastatic murine cancer cell line (LuM1), its MMP3-KO subline, LuM1pToma, RAW264.7 macrophages, and THP-1 monocytic cells were maintained in RPMI1640 medium supplemented with 10% FBS, penicillin, streptomycin, and amphotericin [32]. THP1 cells were differentiated into macrophages by treating with 200 nM phorbol 12-myristate 13-acetate (PMA) and 50 mM 2-mercaptoethanol (2ME). Cells were cultured in a humidified incubator at 37°C with 5% CO_2.

Murine oral carcinoma (MOC) cell lines (MOC1; KER-EWL001-FP, MOC2; KER-EWL002-FP) were purchased from a Kerafast cell bank. These cells were cultured in Iscove's modified Dulbecco's medium (IMDM) (Gibco) and Ham's Nutrient Mixture (F12) (Gibco) in a 2:1 ratio with 5% FBS (Gibco), 1% antimycotic-antibiotic solution (Gibco), 5 mg/mL insulin (MilliporeSigma), 400 ng/mL hydrocortisone (MilliporeSigma), and 5 ng/mL EGF (BioLegend, SanDiego, CA, USA) at 37°C in a humidifying incubator with 5% CO_2.

Direct and indirect co-culture

For direct co-culture of mouse cells, both RAW cells and cancer cells (LuM1 or MMP3KO) were seeded at 5 × 10^5 cells/well in a 12-well plate. For indirect co-culture, RAW cells were first seeded, and cancer cells were then seeded into polyethylene terephthalate (PET)-membrane cell culture inserts with 0.1, 0.4 or 1.0-µm pores (Celltreat, Ayer, MA, USA; Corning, Corning, NY, USA) at 5 × 10^5 or 1 × 10^6 cells/well. For human cell co-culture, THP-1 cells were seeded at 5 × 10^5 cells/well in a 12-well plate. 24 hours later, we added PMA and 2ME, then seeded M3 cells (2 × 10^5 cells) in the cell culture inserts or co-cultured them directly. For confocal microscopy, we placed a poly-L-lysine (PLL)-coated 13-mm culture cover glass (Matsunami Glass, Osaka, Japan) on the bottom of the well and then seeded cells.

Chemicals

We used two selective PKM2 inhibitors, shikonin (Cayman, Ann Arbor, MI, USA) and PKM2-IN-1 (Selleck, Houston, TX, USA). PK activator Mitapivat [pyrukynd] (Selleck) and selective PKM2 activator TEPP-46

[ML-265] (Adipgen, San Diego, CA, USA) were used. Chemicals dissolved in DMSO were used at a final concentration of 0.1% DMSO.

mbGLuc reporter assay

M3/mbGLuc cells were seeded at 10,000 cells per well in 200 µL in a 96-well plate. After 24 h, cells were treated with inhibitors or activators by replacing the medium. After 72 h, we collected cell culture supernatants (20 µL) and mixed them with 50 µL of coelenterazine (CTZ) working solution (*Gaussia* luciferase glow kit, Thermo Scientific) in a white 96-well plate. Luminescence was measured in a plate reader Gemini XP SOK (Molecular Devices, San Jose, CA, USA).

MTT assay

For 2D culture, we seeded HSC-3-M3 cells at 3.0 × 10^4 cells per well in 96-well flat-bottom plates. Cells were treated 24 h after seeding with DMEM containing shikonin or PKM2-IN-1 at final concentrations ranging from 10 nM to 100 µM, or mitapivat or TEPP-46 at final concentrations ranging from 1 nM to 10 µM. We assessed cell viability using an MTT Cell-Based Proliferation/Toxicity Assay kit (FineTest, Boulder, CO, USA). For Shikonin, the MTT assay was performed at 24, 48, and 72 h after drug treatment, whereas for PKM2-IN-1, Mitapivat, and TEPP-46, it was performed at 48 h.

3D spheroid culture for the MTT assay was performed as described previously [55]. Cells were seeded at 5.0 × 10^4 cells per well in 96-well round-bottom ULA plates (#7007; Corning, NY, USA). Drug treatment was initiated 48 h after cell seeding. To avoid accidental aspiration of the spheroids, we removed half the medium volume (50 µL) from each well and replaced it with 50 µL of reagent-containing medium. The MTT assay was performed 72 h after drug treatment.

Separation of EVs

For EV separation, the phosphatidylserine (PS)-based affinity purification (AP) method or the modified precipitation-based purification (P) method was combined with the filter concentration (FC) method [9, 56, 57]. For 2D culture, cells were cultured in a 100-mm or 150-mm dish in fresh Essential 8 medium (15 mL per 150-mm dish). Culture supernatants were collected at proliferative, subconfluent and overconfluent stages every other day. For 3D culture, cells were seeded on a 10-cm ULA dish at 1.0 × 10^6 cells/8 mL in mTeSR1 medium and cultured for 6 days. Tumoroids were then cultured in mTeSR1 medium for an additional 2 days. The cell culture supernatants were collected and centrifuged at 1200 × *g* for 30 min at 4°C to remove cells and blebbisomes. The supernatant was taken and centrifuged at 10,000 × *g* for 30 min at 4°C. The pellet was dissolved in 100 µL of PBS in a Hydrophobic NoStick Microcentrifuge Tube (SSIbio, Lodi, CA, USA) and used as a large-EV fraction. For the FC method, the supernatant was concentrated by ultrafiltration using Amicon Ultra-15 centrifugal devices (15 mL, 100 kDa; Merck, Burlington, MA) or Vivaspin 20 (100,000 MWCO PES; Sartorius, Göttingen, Germany) by

centrifugation at 6000 × *g* and 4°C for 15–60 min, several times in a fixed-angle rotor. For example, 40 mL was concentrated to 1 mL. For the AP method, the concentrate was applied to MagCapture EV Isolation Kit PS for HTS (Fujifilm/Wako Pure Chemicals, Osaka, Japan) using a KingFisher Flex System (Thermo Scientific) or Auto-Pure Mini (Bio Medical Science, Tokyo, Japan). For the P method, the concentrate was incubated with an equal volume of Total Exosome Isolation Reagent (Thermo Scientific) at 4°C overnight, then centrifuged at 10,000 × *g* for 60 min to precipitate EVs. The small EV fractions were dissolved in 100 µL of PBS in a Hydrophobic NoStick Microcentrifuge Tube. The protein concentration was measured using a microBCA Protein Assay Kit (Thermo Scientific).

Transmission electron microscopy (TEM)

TEM grids (formvar/carbon-supported copper grids with a 400-mesh grid size) were hydrophilically treated. The EV suspensions (5–10 µL each) were placed on Parafilm. The grids were floated on the EV suspension for 15 min. Samples were treated with a 2% uranyl acetate solution for negative staining for 2 min and visualized at magnifications of 5,000×, 10,000×, or 20,000× with an H-7650 TEM (Hitachi, Tokyo, Japan) at the Central Research Laboratory, Okayama University Medical School.

Particle diameter distribution

The particle diameters of the EV fractions in the range of 0–6000 nm were analyzed based on dynamic light scattering (DLS) using a Zetasizer Nano ZSP (Malvern Panalytical, Malvern, UK).

Proteomics

Proteomes were analyzed using liquid chromatography–tandem mass spectrometry (LC-MS/MS). In the 2D culture experiments, cells were cultured in Essential 8 medium, EVs were separated using the FC-P method, and samples were analyzed using data-independent acquisition (DIA)-based proteomics. After reduction with 10 mM TCEP at 37°C for 30 min in PBS with 2% SDS and alkylation with 50 mM iodoacetamide at ambient temperature for 45 min, protein samples were digested with Trypsin/Lys-C Mix (Promega) at 47°C for 2 hours on S-Trap columns (ProtiFi, NY, USA). The resulting peptides were analyzed using an Orbitrap Exploris 240 mass spectrometer (Thermo Scientific) coupled to an UltiMate 3000 RSLC nano-flow HPLC (Thermo Scientific). Peptides were enriched with µ-Precolumn (0.3 mm i.d. × 5 mm, 5 µm, Thermo Scientific) and separated on an AURORA column (0.075 mm i.d. × 250 mm, 1.6 µm, Ion Opticks Pty Ltd, Australia) using a two-step gradient: 5–40% acetonitrile for 52 min, followed by 40–95% acetonitrile for 2 min in the presence of 0.1% formic acid. The analytical parameters for the Full MS scan were set as follows: Orbitrap Resolution = 11,250; Scan range (m/z) = 495–745; Normalized AGC Target = 300%; Maximum injection time = 23 msec. The analytical parameters for DIA were set as follows; Precursor Mass Range (m/z) = 500–740, DIA Window Type = Auto, Isolation Window (m/z) = 4, Window Overlap (m/z) = 0, Number of Scan Events = 60, HCD Collision Energy = 30%, Orbitrap Resolution = 45,000, MS2 Scan Range (m/z) = 200–1800, Normalized AGC Target = 300%, Maximum Injection Time = 77 msec. The mass spectrometric raw data files were converted to the mzML format using the msconvert software (ProteoWizard). The resulting mzML files were analyzed using DIA-NN 1.9.2. Protein identification and quantification by DIA-NN were performed with mainly default search settings, except

for the precursor m/z range = 500–740 and fragment ion m/z range = 200–1800. The *Homo sapiens* protein sequence database in UniProt was used for the "FASTA digest for library-free search" function. The peptide identification filter was set at Precursor FDR (false discovery rate) < 1%. Glycolytic enzymes were selected. Log2 values of MS scores were calculated. EV protein expression levels were normalized by dividing by the CD9 expression level.

In the 3D culture experiments, tumoroids were cultured in mTeSR1 medium, EVs were separated using FC-P methods, and the samples were analyzed by data-dependent acquisition (DDA)-based proteomics, as described previously [30]. The proteins were digested using an In-Gel Tryptic Digestion Kit (Thermo Scientific). The gel pieces were destained with a mixture of ammonium bicarbonate and acetonitrile. The protein samples were reduced with 50 mM Tris [2-carboxyethyl] phosphine and alkylated with iodoacetamide. To shrink the gel fragments, acetonitrile was added, and the mixture was incubated for 15 min at room temperature (RT). The acetonitrile was then removed, and the gel pieces were air-dried for 5–10 min. Ten microliters of MS-grade trypsin (Pierce, Thermo Scientific) at 0.1 mg/mL was added to the air-dried sample and incubated at RT for 15 min. Ammonium bicarbonate (25 mM final concentration) was added to the sample, which was then digested overnight at 30°C, and the extract was recovered. Next, a 1% formic acid solution was added to the gel pieces, which were incubated for 5 min, and the supernatant was collected as the extract. Extracts containing digested peptides were measured by an Agilent 6330 Ion Trap LC/MS System (Agilent Technologies, Santa Clara, CA, USA) with the MASCOT database search engine at the Central Research Laboratory, Okayama University Medical School. The scores were defined by amino acid sequence coverage rate and fragment frequency. The MS and MS/MS data were analyzed by Spectrum Mill (Agilent Technologies). The protein cutoff score was 8.0. Heat maps were generated using GraphPad Prism (GraphPad Software, Boston, MA, USA).

RNA isolation, RNA-seq, and pathway analysis

For multi-omics of tumoroids, cells were seeded into 10-cm ultra-low-attachment (ULA) dishes (5 dishes per condition) (Greiner, Kremsmunster, Austria) at a density of 1.0 × 10^6 cells in 8 mL of mTeSR1 medium (StemCell Technologies, Vancouver, BC, Canada) and cultured for 6 days [33]. Cells were then cultured in mTeSR1 medium for an additional 2 days before sampling.

EVs were separated using the above-mentioned FC-P method. Total RNA from EVs was extracted using the Total Exosome RNA Isolation Kit (Thermo Scientific). For RNA isolation from tumoroids, pellets were directly lysed in 1 mL TRIzol™ reagent (Invitrogen/Thermo Scientific) by pipetting up and down to homogenize. Chloroform (Sigma-Aldrich; 0.2 mL per 1 mL TRIzol) was added, and samples were vigorously shaken, incubated for 2–3 min, and centrifuged at 12,000 × *g* for 15 min at 4°C. The upper aqueous phase was transferred to a new tube, and RNA was precipitated with 0.5 mL isopropanol (Sigma-Aldrich) per 1 mL TRIzol, then incubated for 10 min at RT and centrifuged at 12,000 × *g* for 15 min at 4°C. The pellet was washed with 1 mL of 75% ethanol (Sigma-Aldrich), vortexed briefly, and centrifuged at 7,500 × *g* for 5 min at 4°C. After removing the supernatant, the pellet was air-dried for 10–15 min and resuspended in 50 µL RNase-free water preheated to 60°C. Samples were incubated at 60°C for 10 min to aid dissolution.

Genomic DNA contamination was removed by DNase I treatment using recombinant DNase I (New England Biolabs, Ipswich, MA, USA) in the presence of RNase inhibitor. DNase-treated RNA was purified using Monarch RNA Cleanup Kits (New England Biolabs). RNA concentration was determined using the Qubit RNA High Sensitivity Assay Kit (Thermo Scientific). RNA integrity was assessed using Bioanalyzer 2100 and Agilent High Sensitivity RNA ScreenTape (Agilent Technologies, Santa Clara, CA, USA). Only RNA samples with sufficient yield and RNA integrity number (RIN) ≥ 7, or equivalent quality metrics, were used for library preparation.

RNA-seq libraries were prepared using the NEB Next Ultra II Directional RNA Library Prep Kit (New England Biolabs) according to the manufacturer's instructions. For EV samples, poly(A)+ mRNA enrichment was applied directly because rRNA was absent. In contrast, for oncosphere/tumoroid samples, rRNA depletion was performed prior to mRNA enrichment. Library preparation included RNA fragmentation, first- and second-strand cDNA synthesis, end repair and dA-tailing, ligation of indexed adapters, user enzyme digestion, size selection using SPRI-based beads, and PCR amplification. Library quality and fragment size distribution were evaluated using the Agilent 2200 TapeStation system with the High Sensitivity D1000 ScreenTape (Agilent), and library concentrations were quantified using Qubit. Libraries were pooled at equimolar concentrations and sequenced on an Illumina HiSeq/MiSeq sequencer platform using 2 × 150 bp paired-end chemistry, generating approximately 20–40 million reads per sample. Sequencing data were processed using standard bioinformatic pipelines, including quality filtering, alignment to the reference genome, and downstream expression analysis.

Differentially expressed genes (DEGs) (Log2 fold changes > 1) were selected for further analysis. We analyzed KEGG pathways using DAVID Bioinformatics Resources 6.8 and presented a bubble plot generated using R (3.6.2).

Flow cytometry (FCM)

Flow cytometry of EVs was performed using a CytoFLEX S flow cytometer (Beckman Coulter, Indianapolis, Indiana) in accordance with guidelines [9, 58]. For the size standard, we used the Nano Fluorescent Size Standard Kit, Yellow, Flow Cytometry Grade, including 0.20, 0.45, 0.88, and 1.26 μm beads (Spherotech, Lake Forest, IL, USA). EVs were isolated using the FC-AP method. SEVs or LEVs (1 or 2 μL) were diluted in 100 μL of PBS in Hydrophobic NoStick Microcentrifuge Tubes. For the Triton test, 2 μL of EV fraction and 10 μL of 10% Triton X-100 were mixed in 100 μL of PBS and vortexed overnight. In the CytoFLEX, the detector configuration setting of V450 was changed from 450/45 to 405/10 nm for VSCC, and the channels V525 (violet 405 nm laser and bandpass filter 525/40) and Y585 (yellow-green 561 nm laser and bandpass filter 585/42) were used to detect green autofluorescence and tdTomato, respectively. The sample flow rate was set to slow (10 μL/min) or medium (30 μL/min). The event number was automatically counted and recorded as the EV number. The data were acquired and analyzed using CytExpert 2.5 (Beckman Coulter).

Quantitative immunocytochemistry (qICC) and confocal microscopy

THP-1 cells (5 ×10^5 cells/well) were cultured with PMA and 2ME in 8-well chamber slides (Falcon, Corning, NY, USA) overnight. The medium was replaced with RPMI medium (200 μL/well) containing SEV or LEV fractions (4 μL). Cells were cultured for 2 days. Direct and indirect co-cultures were performed for 2 days. ICC was performed as previously described [30]. Cells were washed with PBS and fixed in 4% paraformaldehyde (PFA) for 10 min. Cells were washed three times with PBS for 3 min each. Cells were permeabilized with 0.2% Triton X-100 for 10 min and washed 3 times with PBS for 3 min each. Cells were blocked with Blocking One Histo (Nacalai Tesque, Kyoto, Japan) for 10 min and washed with PBS for 5 min. Cells were incubated with primary antibodies (Table S1) in 1:20-diluted Blocking One Histo in PBS overnight at 4℃. Cells were washed with PBS for 3 min, 3 times. Cells were incubated with Alexa Fluor secondary antibodies (Table S2) in 1:20-diluted Blocking One Histo in PBS for 1 hour at RT. Cells were washed with PBS for 3 min, 3 times. Cells were mounted with mounting medium containing DAPI (Abcam, Cambridge, UK). Fluorescence images were taken using the BZ-X800 all-in-one fluorescence microscope (Keyence, Osaka, Japan) with a ×10 lens (for quantification), a ×20 or ×40 lens (for representative images), and haze reduction (level 1 or 2).

For quantitative ICC, we acquired three to six fields-of-view ICC images using the BZ-X800 microscope (Keyence) with ×10 lenses and analyzed them using the hybrid cell count tool in a BZ-X800 analyzer (Keyence). Exposure time and cut-off values were: 1/100–200 sec and auto (around 100) for DAPI; 1/2.5 sec and 2000 for MRC1; 1/2.5 sec and 500 for pPKM2; 1/3 sec and 300 for NOS2; 1/2.5 sec and 400 for MMP3. Positively stained cell number, positive area (μm^2), and expression (brightness) in each field were divided by the number of DAPI-positive cells. Representative images of THP-1 cells were captured using a ×40 lens with exposure times of 1/400 sec (DAPI), 1/50 sec (MRC1), 1/30 sec (NOS2), and 1 sec (pTomato).

Confocal images were taken using the LSM780 confocal laser scanning microscope (CLSM) (Carl Zeiss, Oberkochen, Germany) at the Central Research Laboratory, Okayama University Medical School, with a ×63 oil immersion lens, diode laser (405 nm, blue), argon laser (488 nm, green), HeNe laser (594 nm, red), 1-μm section, pinhole 65–70, averaging 4, and size setting 1280 × 1280 pixels. Brightness, contrast, gamma, pseudo-colors, and image merge were adjusted using ZEN 3.0 SR black edition (Carl Zeiss).

Orthotopic OSCC mouse models

Tumor allografts were performed on the right buccal mucosa of wild-type female C57/6J mice at a concentration of 3×10^4 cells/50 μL Hank's Balanced Salt Solution (HBSS) (Invitrogen, Thermo Scientific) for MOC2 cells and a 2×10^6 cells/60 μL 1:3 ratio of Matrigel (Corning) to HBSS for MOC1, as described previously [59]. Mice were sacrificed at 3 weeks after MOC2 transplantation and 4 weeks after MOC1 transplantation.

Immunohistochemistry (IHC) and Image analysis

Endogenous peroxidase activity was blocked using 1.2% hydrogen peroxide (Sigma) in methanol. The antigen retrieval was performed according to the manufacturer’s instructions. Primary antibodies used

were listed in Table S1. Tissue sections were incubated with a protein blocking solution for 30 min at RT, followed by incubation with the primary antibody at 4°C overnight. After washing with Tris-Buffered Saline (TBS), sections were incubated with a secondary antibody for 1 hour at RT and then treated with an avidin-biotin complex for 30 min. Color was developed using 3,3'-diaminobenzidine (DAB). Counterstaining was performed using Mayer's hematoxylin. Stained sections were observed under an optical microscope (BX53, Olympus). For each group, five representative images were acquired per animal.

The number of positively stained cells was counted and quantified using ImageJ2 software (version 2.16). Digital image analysis was performed using QuPath (version 0.7.0 x64). We detected cells using the built-in watershed algorithm with a detection threshold of 0.04 and a cell expansion of 3 px, and measured the mean DAB optical density (OD) separately in the nuclear and cytoplasmic compartments of each detected cell. Cells were classified by staining intensity as negative (OD < 0.1), weak (0.1–0.2), moderate (0.2–0.4), or strong (> 0.4), and an H-score was calculated for each image as (%weak × 1) + (%moderate × 2) + (%strong × 3), with nuclear and cytoplasmic H-scores calculated separately. To account for non-specific background staining, we also calculated a background-corrected H-score by subtracting the 10th percentile of the DAB OD distribution for each image from all values before reclassification and recalculation.

Single-cell RNA-sequencing (scRNA-seq) analysis

Publicly available HNSC scRNA-seq data were obtained from the Gene Expression Omnibus (accession number: GSE181919), as previously reported [60]. The author-provided UMI count matrix and cell annotations were used to examine gene expression across annotated cell types in human papillomavirus (HPV)-negative patients. Primary tumors were further classified based on their anatomical site. Analyses were performed in R 4.4.3 using ggplot2, irlba, uwot, and scales.

Patient-derived sample analysis

We performed Pan-cancer analysis of PKM mRNA expression using the Human Protein Atlas (https://www.proteinatlas.org). Comparisons between tumors and paired normal tissues were performed using GEPIA (http://gepia.cancer-pku.cn) for mRNA expression and UALCAN (https://ualcan.path.uab.edu/) for protein expression [61]. Kaplan-Meier (KM) survival curves were generated using the KM plotter (https://kmplot.com) with the TCGA database [61].

Statistical analysis

Statistical significance analyses and graph generation were performed using Prism 11 (GraphPad Software) and Excel (Microsoft). We compared two groups using a two-tailed unpaired or paired t-test, as appropriate. Three or more groups were compared using a one-way ANOVA with Tukey's multiple comparison test. In the quantitative IHC, data were non-normally distributed, as assessed by the Shapiro–Wilk test; differences between MOC1 and MOC2 were therefore evaluated using the Mann–Whitney U test (Wilcoxon rank-sum) (unpaired, two-tailed). For KM analysis, we assessed statistical

significance using the log-rank test and calculated log-rank p-values and hazard ratios (HRs) using KM Plotter. Statistical significance was set at $p < 0.05$. Data were expressed as mean ± the standard error of the mean (s.e.m.) unless otherwise specified.

Abbreviations

AP	affinity purification
COAD	colon adenocarcinoma
CRC	colorectal cancer
E8	Essential 8
ENO1	enolase 1
EV	extracellular vesicle
FC	filter concentration
HNSC	head and neck squamous cell carcinoma
HR	hazard ratio
LC-MS/MS	liquid chromatography – tandem mass spectrometry
LEV	large extracellular vesicle
LN	lymph node
LuM1	lung metastatic colon cancer cell line 1
mbGluc	membrane-bound *Gaussia* luciferase
MMP	matrix metalloproteinase
MOC	mouse oral carcinoma cell line
MRC1	mannose receptor C-type 1 (CD206)
NOS2	nitric oxide synthase 2 / induced NOS (iNOS)
OSCC	oral squamous cell carcinoma
P	precipitation-based purification
PAAD	pancreatic adenocarcinoma

PGK1	phosphoglycerate kinase 1
PKM	pyruvate kinase, muscle-type
READ	renal adenocarcinoma
SEV	small extracellular vesicle
TAM	tumor-associated macrophage
TM	transmembrane
TME	tumor microenvironment

Declarations

Availability of data and materials: The datasets generated in the current study are available from the corresponding author upon reasonable request.

Acknowledgments: The authors thank Tomohiro Inoue and all laboratory members for technical assistance and discussions; Yuka Okusha for generating CRISPR/Cas9-based MMP3-KO cells; Moemi Tshukano for EM; Yukinari Isomoto for support with FCM; and Testushi Iwasa for support with Confocal microscopy. Schematic illustrations were created using BioRender and PowerPoint.

Authors' contributions: Conceptualization, T.E.; Methodology, T.E., K.U., H.S.E., C.S., H.K., K.Y., M.S., Y.L. and M.W.O.; Investigation, K.Y. (cell culture, MTT, and reporter assays), C.S. and E.A.T. (3D culture, EV separation, DDA proteomics, EV RNA isolation, library construction, and RNA-seq), Y.W. (scRNA-seq analysis), M.S. (bubble plots, variant analysis), L.X. (establishment and application of mbGluc reporter assay), H.S. (DIA proteomics), H.S.E. (qIHC), T.E. (cell culture, EV separation, TEM, DLS, FCM, coculture, ICC, dry analyses, heatmap generation); Validation, M.W.O. (Dry analyses of RNA-seq), T.E. (database analyses), M.S. (MTT assay); Data curation, T.E. K.Y., L.X., H.S.E. and K.U.; Formal analysis, T.E., H.S.E. and K.Y.; Funding acquisition, T.E., M.S., K.Y., Y.L., H.K. and K.U.; Resources, T.E. (cell models, automated EV separation system, Keyence microscope), K.U. (proteomics system) and H.K. (patient-derived specimens); Writing—original draft preparation, T.E., E.A.T., H.S.E., K.U., K.Y., and M.W.O.; Writing—review and editing, T.E., Y.W. and E.A.T.; Visualization, T.E. (illustration); Supervision, T.E., C.S., K.Y., K.O., H.K. and K.U.; Project administration, T.E.; All authors have read and agreed to the manuscript.

Competing interests: The authors declare no competing interests.

Ethics approval and consent to participate

The study was approved by the Okayama University Human Ethics Committee (Approval number: 1608–018), and informed consent was obtained from all patients.

Consent for publication: Not applicable

Fundings: This research was funded by the Japan Society for the Promotion of Science (JSPS) under Kakenhi 26K02814 (to T.E., K.U., H.K.), 26K23766 (to T.E., H.K.), 23K28000 (to T.E., H.K.), 22KF0268 (to T.E., M.S.), 25K02812 (to T.Y., T.E.), 24K13239 (to K.O., T.E.) and 24K19860 (to K.Y.); the Japan Science and Technology Agency (JST) under LOTUS Programme (to T.E., V.M.); the Wesco Scientific Promotion Foundation (to T.E.).

Declaration of generative AI and AI-assisted technologies: We used Gemini Notebook to generate the graphical abstract based on our draft.

References

1. Mody MD, Rocco JW, Yom SS, Haddad RI, Saba NF: Head and neck cancer. *Lancet* 2021, 398(10318):2289–2299.
2. Bray F, Laversanne M, Sung H, Ferlay J, Siegel RL, Soerjomataram I, Jemal A: Global cancer statistics 2022: GLOBOCAN estimates of incidence and mortality worldwide for 36 cancers in 185 countries. *CA Cancer J Clin* 2024, 74(3):229–263.
3. Sung H, Ferlay J, Siegel RL, Laversanne M, Soerjomataram I, Jemal A, Bray F: Global Cancer Statistics 2020: GLOBOCAN Estimates of Incidence and Mortality Worldwide for 36 Cancers in 185 Countries. *CA Cancer J Clin* 2021, 71(3):209–249.
4. Johnson DE, Burtness B, Leemans CR, Lui VWY, Bauman JE, Grandis JR: Head and neck squamous cell carcinoma. *Nat Rev Dis Primers* 2020, 6(1):92.
5. Sano D, Myers JN: Metastasis of squamous cell carcinoma of the oral tongue. *Cancer Metastasis Rev* 2007, 26(3–4):645–662.
6. Okano S, Homma A, Kiyota N, Tahara M, Hanai N, Asakage T, Matsuura K, Ogawa T, Saito Y, Sano D *et al*: Induction chemotherapy in locally advanced squamous cell carcinoma of the head and neck. *Jpn J Clin Oncol* 2021, 51(2):173–179.
7. Psaila B, Lyden D: The metastatic niche: adapting the foreign soil. *Nat Rev Cancer* 2009, 9(4):285–293.
8. Sheta M, Taha EA, Lu Y, Eguchi T: Extracellular Vesicles: New Classification and Tumor Immunosuppression. *Biology (Basel)* 2023, 12(1).
9. Welsh JA, Goberdhan DCI, O'Driscoll L, Buzas EI, Blenkiron C, Bussolati B, Cai H, Di Vizio D, Driedonks TAP, Erdbrugger U *et al*: Minimal information for studies of extracellular vesicles (MISEV2023): From basic to advanced approaches. *J Extracell Vesicles* 2024, 13(2):e12404.
10. D'Souza-Schorey C, Di Vizio D: A class of large cell-like extracellular vesicles. *Nat Cell Biol* 2025, 27(3):372–374.
11. Heidarzadeh M, Zarebkohan A, Rahbarghazi R, Sokullu E: Protein corona and exosomes: new challenges and prospects. *Cell Commun Signal* 2023, 21(1):64.

12. Toth EA, Turiak L, Visnovitz T, Cserep C, Mazlo A, Sodar BW, Forsonits AI, Petovari G, Sebestyen A, Komlosi Z *et al*: Formation of a protein corona on the surface of extracellular vesicles in blood plasma. *J Extracell Vesicles* 2021, 10(11):e12140.
13. Valadi H, Ekstrom K, Bossios A, Sjostrand M, Lee JJ, Lotvall JO: Exosome-mediated transfer of mRNAs and microRNAs is a novel mechanism of genetic exchange between cells. *Nat Cell Biol* 2007, 9(6):654–659.
14. Raposo G, Stoorvogel W: Extracellular vesicles: exosomes, microvesicles, and friends. *J Cell Biol* 2013, 200(4):373–383.
15. Peinado H, Zhang H, Matei IR, Costa-Silva B, Hoshino A, Rodrigues G, Psaila B, Kaplan RN, Bromberg JF, Kang Y *et al*: Pre-metastatic niches: organ-specific homes for metastases. *Nat Rev Cancer* 2017, 17(5):302–317.
16. Eguchi T, Sheta M, Fujii M, Calderwood SK: Cancer extracellular vesicles, tumoroid models, and tumor microenvironment. *Semin Cancer Biol* 2022, 86(Pt 1):112–126.
17. Ono K, Sogawa C, Kawai H, Tran MT, Taha EA, Lu Y, Oo MW, Okusha Y, Okamura H, Ibaragi S *et al*: Triple knockdown of CDC37, HSP90-alpha and HSP90-beta diminishes extracellular vesicles-driven malignancy events and macrophage M2 polarization in oral cancer. *J Extracell Vesicles* 2020, 9(1):1769373.
18. Fujiwara T, Eguchi T, Sogawa C, Ono K, Murakami J, Ibaragi S, Asaumi JI, Calderwood SK, Okamoto K, Kozaki KI: Carcinogenic epithelial-mesenchymal transition initiated by oral cancer exosomes is inhibited by anti-EGFR antibody cetuximab. *Oral Oncol* 2018, 86:251–257.
19. Gatenby RA, Gillies RJ: Why do cancers have high aerobic glycolysis? *Nat Rev Cancer* 2004, 4(11):891–899.
20. Devic S: Warburg Effect - a Consequence or the Cause of Carcinogenesis? *J Cancer* 2016, 7(7):817–822.
21. Dong G, Mao Q, Xia W, Xu Y, Wang J, Xu L, Jiang F: PKM2 and cancer: The function of PKM2 beyond glycolysis. *Oncol Lett* 2016, 11(3):1980–1986.
22. Dayton TL, Jacks T, Vander Heiden MG: PKM2, cancer metabolism, and the road ahead. *EMBO Rep* 2016, 17(12):1721–1730.
23. Luan W, Wang Y, Chen X, Shi Y, Wang J, Zhang J, Qian J, Li R, Tao T, Wei W *et al*: PKM2 promotes glucose metabolism and cell growth in gliomas through a mechanism involving a let-7a/c-Myc/hnRNPA1 feedback loop. *Oncotarget* 2015, 6(15):13006–13018.
24. Zahra K, Dey T, Ashish, Mishra SP, Pandey U: Pyruvate Kinase M2 and Cancer: The Role of PKM2 in Promoting Tumorigenesis. *Front Oncol* 2020, 10:159.
25. Gao L, Yang F, Tang D, Xu Z, Tang Y, Yang D, Sun D, Chen Z, Teng Y: Mediation of PKM2-dependent glycolytic and non-glycolytic pathways by ENO2 in head and neck cancer development. *J Exp Clin Cancer Res* 2023, 42(1):1.
26. Hey S, Linder S: Matrix metalloproteinases at a glance. *J Cell Sci* 2024, 137(2).

27. Bassiouni W, Ali MAM, Schulz R: Multifunctional intracellular matrix metalloproteinases: implications in disease. *FEBS J* 2021, 288(24):7162–7182.
28. Mannello F, Medda V: Nuclear localization of matrix metalloproteinases. *Prog Histochem Cytochem* 2012, 47(1):27–58.
29. Eguchi T, Kubota S, Kawata K, Mukudai Y, Uehara J, Ohgawara T, Ibaragi S, Sasaki A, Kuboki T, Takigawa M: Novel transcription-factor-like function of human matrix metalloproteinase 3 regulating the CTGF/CCN2 gene. *Mol Cell Biol* 2008, 28(7):2391–2413.
30. Eguchi T, Taha EA, Nakano K, Tiwari V, Takebe K, Inoue T, Xing L, Sogawa C, Okamoto K, Calderwood SK: MMP-3 cleavage of Lamin A induces pro-migratory nuclear deformity, nucleophagy, and their autophagic secretion with extracellular vesicles in metastatic cancer. *Cell Commun Signal* 2026, 24(1).
31. Kessenbrock K, Plaks V, Werb Z: Matrix metalloproteinases: regulators of the tumor microenvironment. *Cell* 2010, 141(1):52–67.
32. Okusha Y, Eguchi T, Sogawa C, Okui T, Nakano K, Okamoto K, Kozaki KI: The intranuclear PEX domain of MMP involves proliferation, migration, and metastasis of aggressive adenocarcinoma cells. *J Cell Biochem* 2018, 119(9):7363–7376.
33. Taha EA, Sogawa C, Okusha Y, Kawai H, Oo MW, Elseoudi A, Lu Y, Nagatsuka H, Kubota S, Satoh A *et al*: Knockout of MMP3 Weakens Solid Tumor Organoids and Cancer Extracellular Vesicles. *Cancers (Basel)* 2020, 12(5).
34. Okusha Y, Eguchi T, Tran MT, Sogawa C, Yoshida K, Itagaki M, Taha EA, Ono K, Aoyama E, Okamura H *et al*: Extracellular Vesicles Enriched with Moonlighting Metalloproteinase Are Highly Transmissive, Pro-Tumorigenic, and Trans-Activates Cellular Communication Network Factor (CCN2/CTGF): CRISPR against Cancer. *Cancers (Basel)* 2020, 12(4).
35. Eguchi T, Sogawa C, Okusha Y, Uchibe K, Iinuma R, Ono K, Nakano K, Murakami J, Itoh M, Arai K *et al*: Organoids with cancer stem cell-like properties secrete exosomes and HSP90 in a 3D nanoenvironment. *PLoS One* 2018, 13(2):e0191109.
36. Sogawa C, Eguchi T, Namba Y, Okusha Y, Aoyama E, Ohyama K, Okamoto K: Gel-Free 3D Tumoroids with Stem Cell Properties Modeling Drug Resistance to Cisplatin and Imatinib in Metastatic Colorectal Cancer. *Cells* 2021, 10(2).
37. Hou PP, Luo LJ, Chen HZ, Chen QT, Bian XL, Wu SF, Zhou JX, Zhao WX, Liu JM, Wang XM *et al*: Ectosomal PKM2 Promotes HCC by Inducing Macrophage Differentiation and Remodeling the Tumor Microenvironment. *Mol Cell* 2020, 78(6):1192–1206 e1110.
38. Yang W, Zheng Y, Xia Y, Ji H, Chen X, Guo F, Lyssiotis CA, Aldape K, Cantley LC, Lu Z: ERK1/2-dependent phosphorylation and nuclear translocation of PKM2 promotes the Warburg effect. *Nat Cell Biol* 2012, 14(12):1295–1304.
39. Lee YJ, Seo CW, Chae S, Lee CY, Kim SS, Shin YH, Park HM, Gho YS, Ryu S, Lee SH *et al*: Metabolic Reprogramming Into a Glycolysis Phenotype Induced by Extracellular Vesicles Derived From Prostate Cancer Cells. *Mol Cell Proteomics* 2025, 24(4):100944.

40. Yin Y, Ming L, Qin Y, Tang J, Liu B, Liu Y, Jin G, Jiang L, Yao S, Qi X *et al*: RAB22A triggers intercellular chemoresistance transmission in colorectal cancer by promoting exosome release via the PKM2-pSNAP23 axis. *Oncogene* 2025, 44(43):4205–4217.
41. Li G, Xiong Z, Li Y, Yan C, Cheng Y, Wang Y, Li J, Dai Z, Zhang D, Du W *et al*: Hypoxic microenvironment-induced exosomes confer temozolomide resistance in glioma through transfer of pyruvate kinase M2. *Discov Oncol* 2024, 15(1):110.
42. Delaveris CS, Loudermilk RP, Pandey A, Remesh SG, Peters-Clarke TM, Ganjave SD, Dougherty WJN, Delavan HM, Wang C, Ling J *et al*: Autophagolysosomal exocytosis inverts Src kinase onto the cell surface in cancer. *Science* 2026, 391(6790):eaec1778.
43. Wang C, Zhang S, Liu J, Tian Y, Ma B, Xu S, Fu Y, Luo Y: Secreted Pyruvate Kinase M2 Promotes Lung Cancer Metastasis through Activating the Integrin Beta1/FAK Signaling Pathway. *Cell Rep* 2020, 30(6):1780–1797 e1786.
44. Brestoff JR, Singh KK, Aquilano K, Becker LB, Berridge MV, Boilard E, Caicedo A, Crewe C, Enriquez JA, Gao J *et al*: Recommendations for mitochondria transfer and transplantation nomenclature and characterization. *Nat Metab* 2025, 7(1):53–67.
45. Jeppesen DK, Sanchez ZC, Kelley NM, Hayes JB, Ambroise J, Koory EN, Krystofiak E, Taneja N, Zhang Q, Dungan MM *et al*: Blebbisomes are large, organelle-rich extracellular vesicles with cell-like properties. *Nat Cell Biol* 2025, 27(3):438–448.
46. Zhang Q, Liu Q, Zheng S, Liu T, Yang L, Han X, Lu X: Shikonin Inhibits Tumor Growth of ESCC by suppressing PKM2 mediated Aerobic Glycolysis and STAT3 Phosphorylation. *J Cancer* 2021, 12(16):4830–4840.
47. Li W, Zhang C, Ren A, Li T, Jin R, Li G, Gu X, Shi R, Zhao Y: Shikonin Suppresses Skin Carcinogenesis via Inhibiting Cell Proliferation. *PLoS One* 2015, 10(5):e0126459.
48. Wang Y, Hao F, Nan Y, Qu L, Na W, Jia C, Chen X: PKM2 Inhibitor Shikonin Overcomes the Cisplatin Resistance in Bladder Cancer by Inducing Necroptosis. *Int J Biol Sci* 2018, 14(13):1883–1891.
49. Xiang T, Wang X, Huang S, Zhou K, Fei S, Zhou B, Yue K, Li Q, Xue S, Dai Y *et al*: Inhibition of PKM2 by shikonin impedes TGF-β1 expression by repressing histone lactylation to alleviate renal fibrosis. *Phytomedicine* 2025, 136:156324.
50. Azoitei N, Becher A, Steinestel K, Rouhi A, Diepold K, Genze F, Simmet T, Seufferlein T: PKM2 promotes tumor angiogenesis by regulating HIF-1alpha through NF-kappaB activation. *Mol Cancer* 2016, 15:3.
51. Hou JY, Wang XL, Chang HJ, Wang XX, Hao SL, Gao Y, Li G, Gao LJ, Zhang FP, Wang ZJ *et al*: PTBP1 crotonylation promotes colorectal cancer progression through alternative splicing-mediated upregulation of the PKM2 gene. *J Transl Med* 2024, 22(1):995.
52. Ma WK, Voss DM, Scharner J, Costa ASH, Lin KT, Jeon HY, Wilkinson JE, Jackson M, Rigo F, Bennett CF *et al*: ASO-Based PKM Splice-Switching Therapy Inhibits Hepatocellular Carcinoma Growth. *Cancer Res* 2022, 82(5):900–915.

53. Lai CP, Mardini O, Ericsson M, Prabhakar S, Maguire C, Chen JW, Tannous BA, Breakefield XO: Dynamic biodistribution of extracellular vesicles in vivo using a multimodal imaging reporter. *ACS Nano* 2014, 8(1):483–494.
54. Zaborowski MP, Lee K, Na YJ, Sammarco A, Zhang X, Iwanicki M, Cheah PS, Lin HY, Zinter M, Chou CY *et al*: Methods for Systematic Identification of Membrane Proteins for Specific Capture of Cancer-Derived Extracellular Vesicles. *Cell Rep* 2019, 27(1):255–268 e256.
55. Ono K, Sato K, Nakamura T, Yoshida Y, Murata S, Yoshida K, Kanemoto H, Umemori K, Kawai H, Obata K *et al*: Reproduction of the Antitumor Effect of Cisplatin and Cetuximab Using a Three-dimensional Spheroid Model in Oral Cancer. *Int J Med Sci* 2022, 19(8):1320–1333.
56. Eguchi T, Okusha Y, Lu Y, Ono K, Taha EA, Fukuoka S: Comprehensive Method for Exosome Isolation and Proteome Analysis for Detection of CCN Factors in/on Exosomes. *Methods Mol Biol* 2023, 2582:59–76.
57. Ono K, Eguchi T, Sogawa C, Calderwood SK, Futagawa J, Kasai T, Seno M, Okamoto K, Sasaki A, Kozaki KI: HSP-enriched properties of extracellular vesicles involve survival of metastatic oral cancer cells. *J Cell Biochem* 2018, 119(9):7350–7362.
58. Welsh JA, Van Der Pol E, Arkesteijn GJA, Bremer M, Brisson A, Coumans F, Dignat-George F, Duggan E, Ghiran I, Giebel B *et al*: MIFlowCyt-EV: a framework for standardized reporting of extracellular vesicle flow cytometry experiments. *J Extracell Vesicles* 2020, 9(1):1713526.
59. Eain HS, Kawai H, Nakayama M, Oo MW, Ohara T, Fukuhara Y, Takabatake K, Shan Q, Soe Y, Ono K *et al*: Double-faced CX3CL1 enhances lymphangiogenesis-dependent metastasis in an aggressive subclone of oral squamous cell carcinoma. *JCI Insight* 2024, 9(10).
60. Choi JH, Lee BS, Jang JY, Lee YS, Kim HJ, Roh J, Shin YS, Woo HG, Kim CH: Single-cell transcriptome profiling of the stepwise progression of head and neck cancer. *Nat Commun* 2023, 14(1):1055.
61. Ono K, Eguchi T: Large-Scale Databases and Portals on Cancer Genome to Analyze Chaperone Genes Correlated to Patient Prognosis. *Methods Mol Biol* 2023, 2693:293–306.

Figures

Fig 1

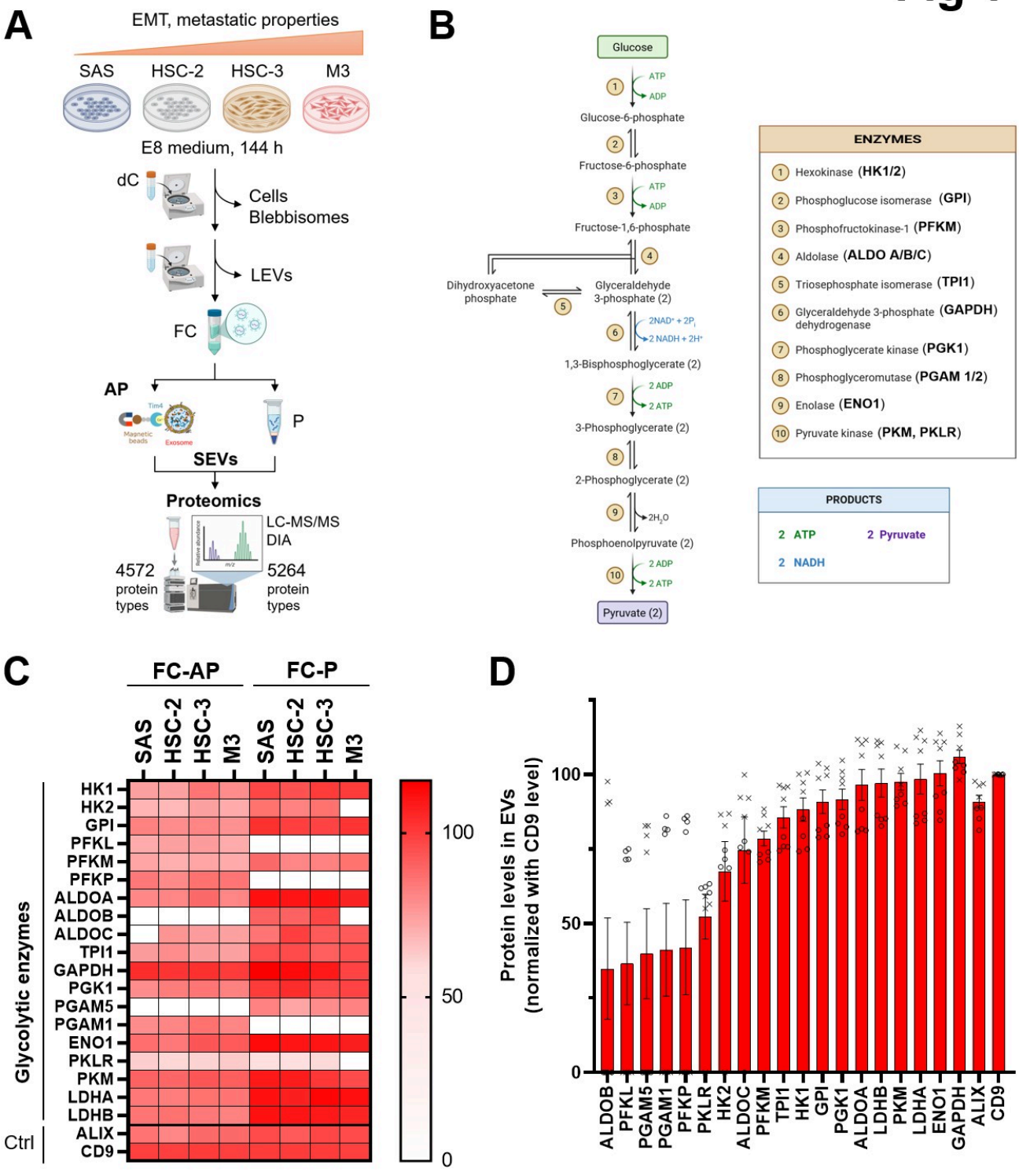


Figure 1

Extracellular vesicles contain the anaerobic glycolytic system in oral cancer. (A) Experimental workflow of EV proteomics. Oral cancer cell lines were cultured in Essential 8 (E8) medium. Small EVs (SEVs) were separated using the FC-AP (filter concentration and affinity purification) and FC-P (FC and precipitation) methods. (B) Anaerobic glycolytic pathway, enzymes, and gene names. (C, D) Heatmap (C) and bar graph (D) showing glycolytic enzymes contained in EVs. Data were normalized to CD9 levels. (C) CD9 and ALIX

were shown at the bottom as controls. (D) Circle plots indicate FC-AP-derived values, and Cross plots indicate FC-P-derived values. (A, B) Illustrations were created using BioRender.

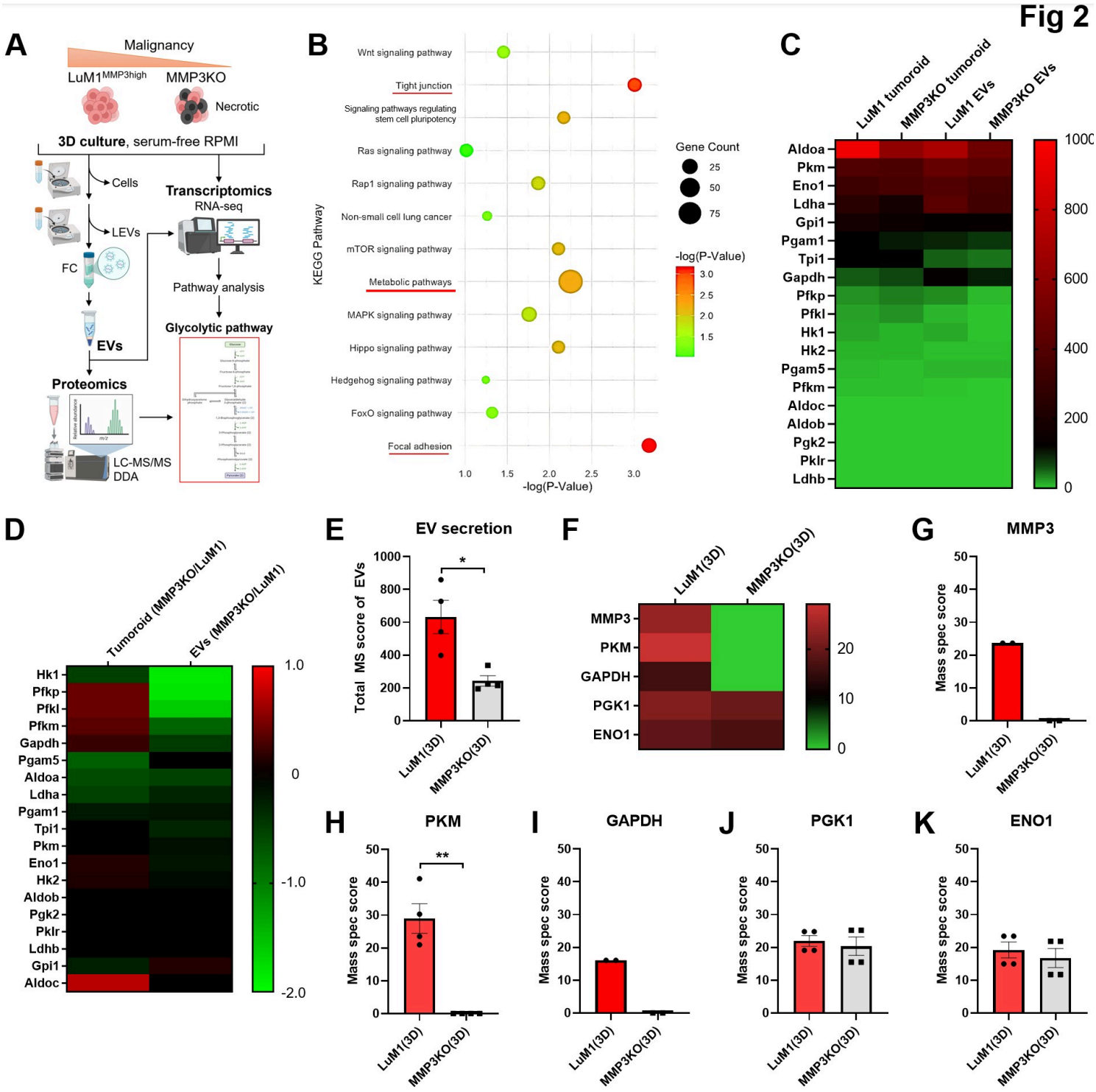


Figure 2

Multi-omics of tumoroid EVs revealed the MMP3-PKM axis regulating glycolytic cargo loading. (A) Experimental flow. LuM1^{MMP3high} and MMP3-KO cells were 3D-cultured in serum-free medium. Multi-omics, including EV transcriptomics and proteomics, revealed changes in the glycolytic pathway. (B) Bubble plot showing pathways altered by MMP3. (C) Heatmap of mRNA expression levels (FPKM) of

glycolytic enzymes in tumoroids and EVs. (D) Heatmap showing altered expression of glycolytic enzyme genes in tumoroids or EVs following MMP3 KO. Values are presented as log2($FPKM^{MMP3KO}/FPKM^{LuM1}$). (E) EV secretion levels evaluated by total mass spectrometry scores. (F) Heatmap showing differential protein abundance in EVs following MMP3-KO. (G–K) Mass spectrometry scores of MMP3 (G), PKM (H), GAPDH (I), PGK1 (J), and ENO1 (K). Mean ± s.e.m., Student's two-tailed paired *t*-test; $*p < 0.05$, $**p < 0.01$ (n = 2–4 LC-MS/MS experiments). (A) Illustrations were created using BioRender.

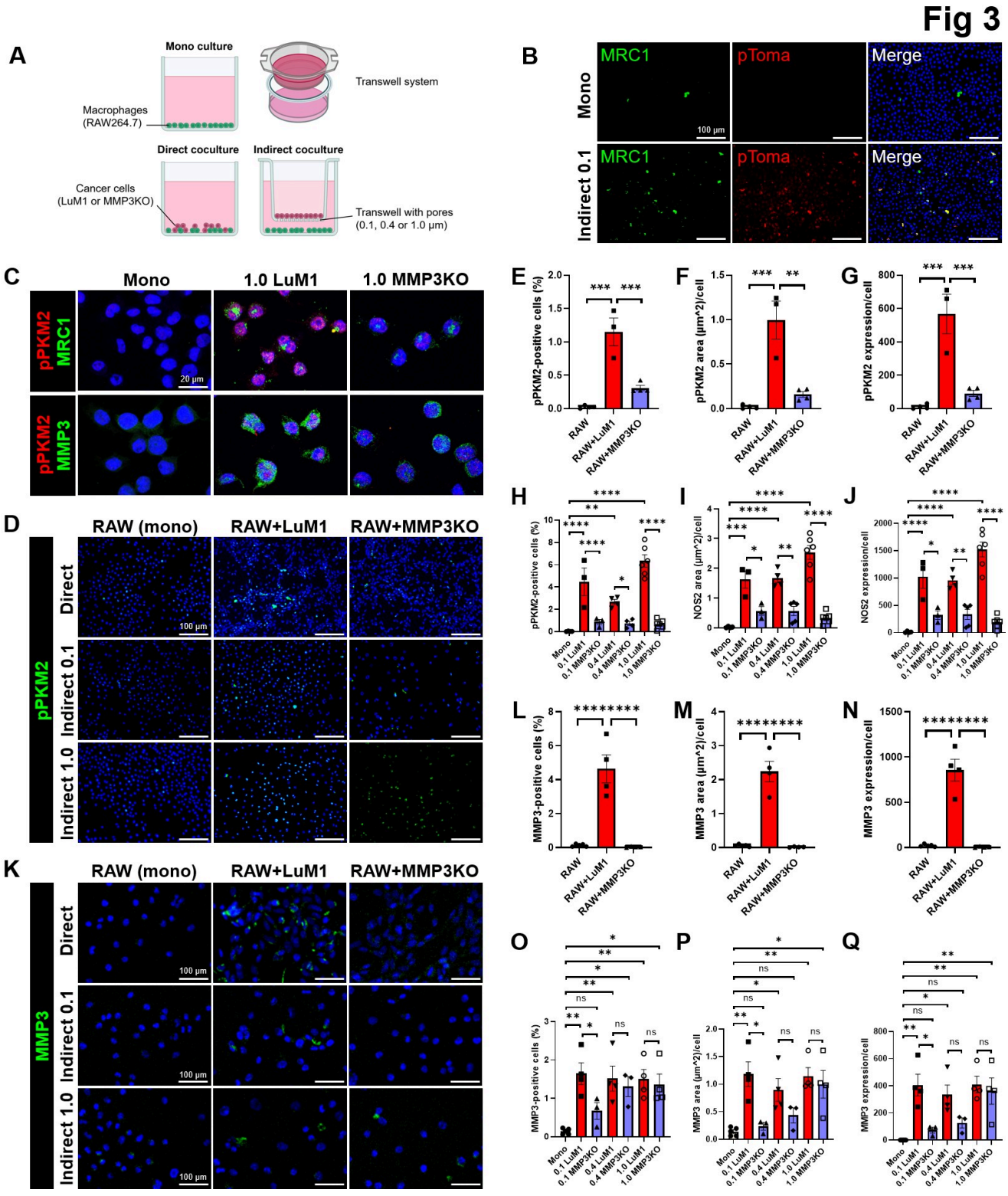


Figure 3

EV-mediated transfer of PKM2 and MMP3 from cancer cells to macrophages. (A) Schematic illustration of monoculture, direct co-culture, and indirect co-culture systems. (B) ICC images of MRC1 and pTomato transferred from LuM1 to RAW264.7 macrophages. (C) Confocal images showing pPKM2, MRC1, and MMP3 in RAW264.7 cells under monoculture and indirect co-culture conditions with LuM1 or MMP3KO cells. (D–J) ICC analysis of pPKM2 in RAW264.7 cells. (D) Representative images; (E–G) direct co-culture, (H–J) indirect co-culture using Transwell inserts with different pore sizes (0.1, 0.4 or 1.0 μm). (K–Q) ICC analysis of MMP3 in RAW264.7 cells. (K) Representative images; (L–N) direct co-culture; (O–Q) Indirect co-culture using Transwell inserts with different pore sizes. Data are presented as mean ± s.e.m. Statistical significance was determined using a one-way ANOVA with Tukey's multiple comparison test; *p < 0.05, **p < 0.01, ***p < 0.001, ****p < 0.0001 (n = 3–6 fields of view).

Fig 4

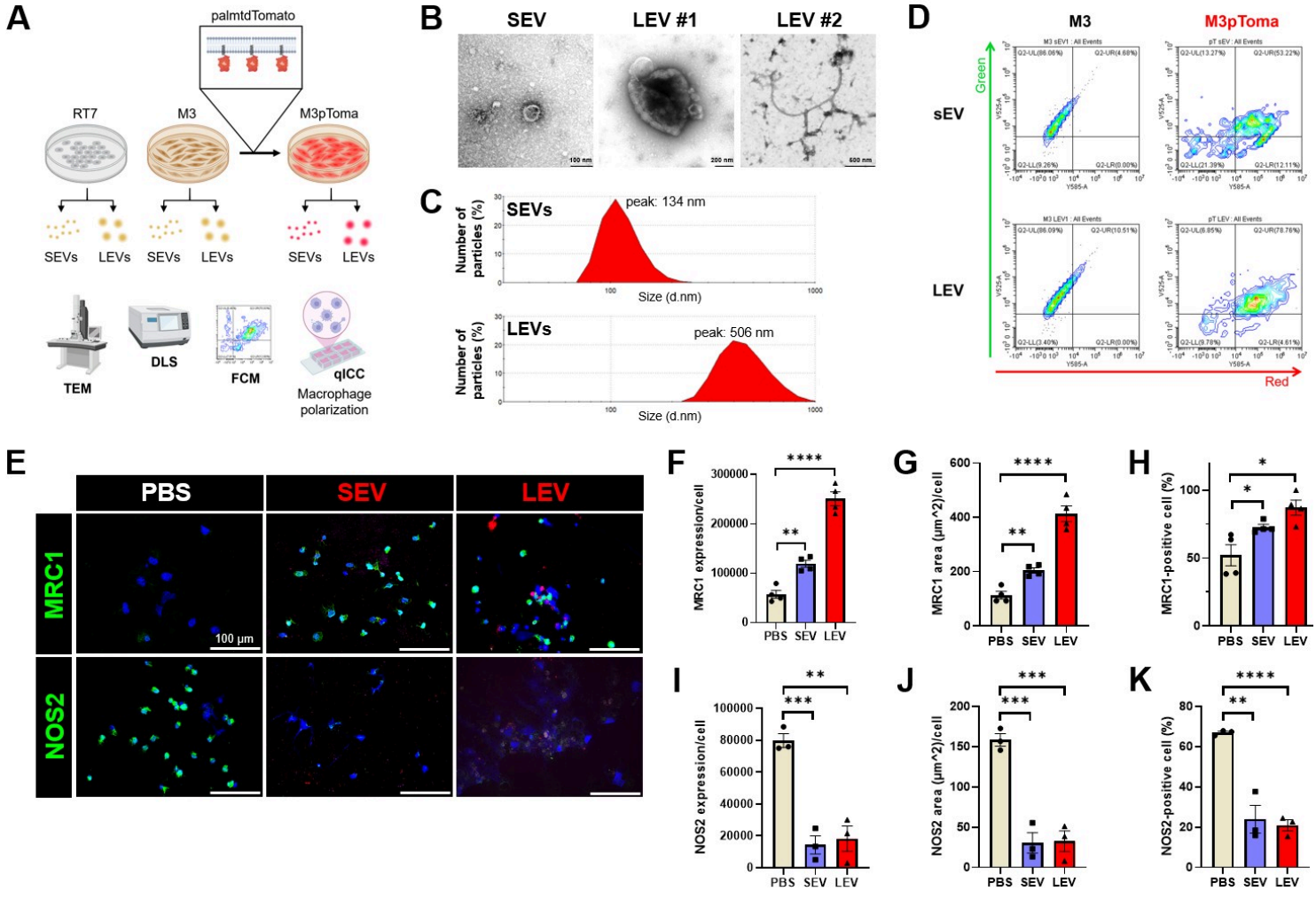


Figure 4

Oral cancer-derived large and small EVs regulate macrophage (TAM) polarization. (A) Schematic illustration showing the methodology. M3pToma cells were established by stably transfecting M3 cells

with the palmtdTomato construct. LEVs were isolated using centrifugation. SEVs were isolated using the FC-AP method. (B) TEM images of a SEV, LEV #1 and LEV #2 (migrasome fragment) from M3 cells. (C) Particle size distribution of M3-derived EVs analyzed using DLS. (D) FCM of SEVs and LEVs from M3 and M3pToma cells. (E–K) qICC analysis of MRC1 and NOS2 in THP-1 cells treated with SEVs and LEVs. (E) Representative ICC images. Scale bars, 100 μm. (F–K) qICC analysis of MRC1 and NOS2 expression (F, I), area/cell (G, J) and positive cell rate (H, K). n = 3–4. Statistical significance was analyzed using a one-way ANOVA with Tukey's multiple comparison test. *p < 0.005, **p < 0.01, ***p < 0.001, and ****p < 0.0001.

Fig 5

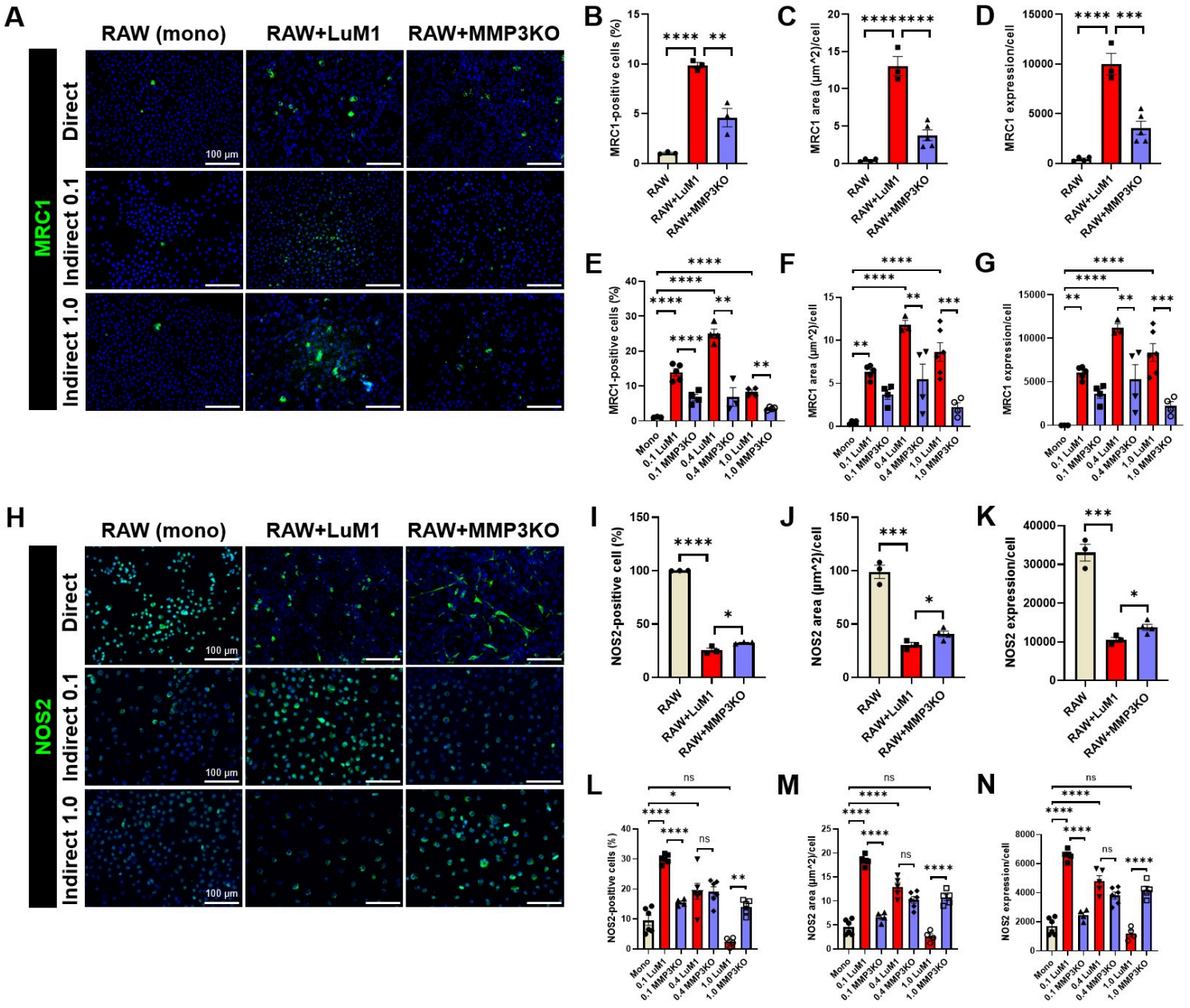


Figure 5

Colon cancer-derived large and small EVs regulate macrophage (TAM) polarization. RAW264.7 macrophages were monocultured or cocultured with LuM1 or MMP3KO cells. (A–G) ICC analysis of MRC1 (CD206) expression in RAW264.7 cells. (A) Representative images; (B–D) direct co-culture; (E–G) indirect co-culture using Transwell inserts with different pore sizes (0.1, 0.4 or 1.0 μm). (H–N) ICC analysis of NOS2 expression in RAW264.7 cells. (H) Representative images; (I–K) direct co-culture; (L–N) indirect co-culture using Transwell inserts with different pore sizes. Data are presented as mean ± s.e.m. Statistical significance was determined using a one-way ANOVA with Tukey's multiple comparison test; *p < 0.05, **p < 0.01, ***p < 0.001, ****p < 0.0001 (n = 3–6 fields of view).

Fig 6

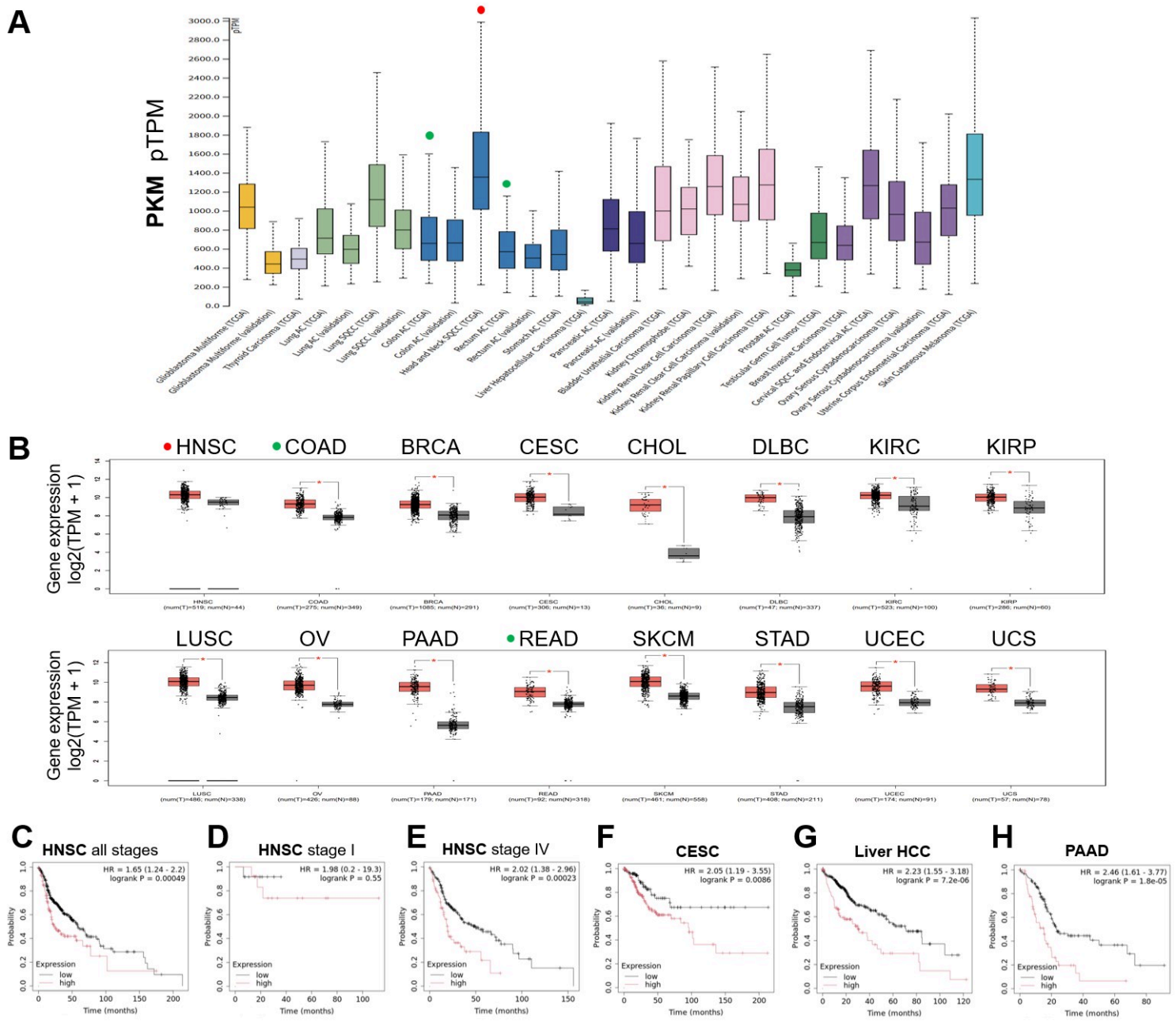


Figure 6

***PKM* gene expression is associated with poor prognosis across multiple cancer types.** (A) *PKM* mRNA expression across multiple cancer types. HNSC is highlighted with a red dot for visualization. (B) Box-and-whisker plot showing differential *PKM* expression in multiple tumor types compared with paired normal tissues. COAD and READ are highlighted with green spots. Mean ± s.e.m. Statistical comparisons were performed using one-way ANOVA; *$p < 0.01$ (sample sizes were indicated in the figure). (C–H) Kaplan-Meier survival analysis comparing patients with high (red) versus low (black) *PKM* expression groups. Statistical significance was assessed using the log-rank test. (C) HNSC, all stages. HR = 1.65. $p = 0.00049$, n = 360 (low), n = 139 (high). (D) Stage I HNSC. HR = 1.98. $p = 0.55$, n = 12 (low), n = 13 (high). (E) Stage IV HNSC. HR = 2.02. $p = 0.00023$, n = 191 (low), n = 68 (high). (F) CESC. HR = 2.05. $p = 0.0086$, n = 108 (low), n = 196 (high). (G) Liver HCC. HR = 2.23. $p = 7.2 \times 10^{\wedge-6}$, n = 275 (low), n = 95 (high). (H) PADD. HR = 2.46. $p = 1.8 \times 10^{\wedge-5}$, n = 126 (low), n = 51 (high).

Fig 7

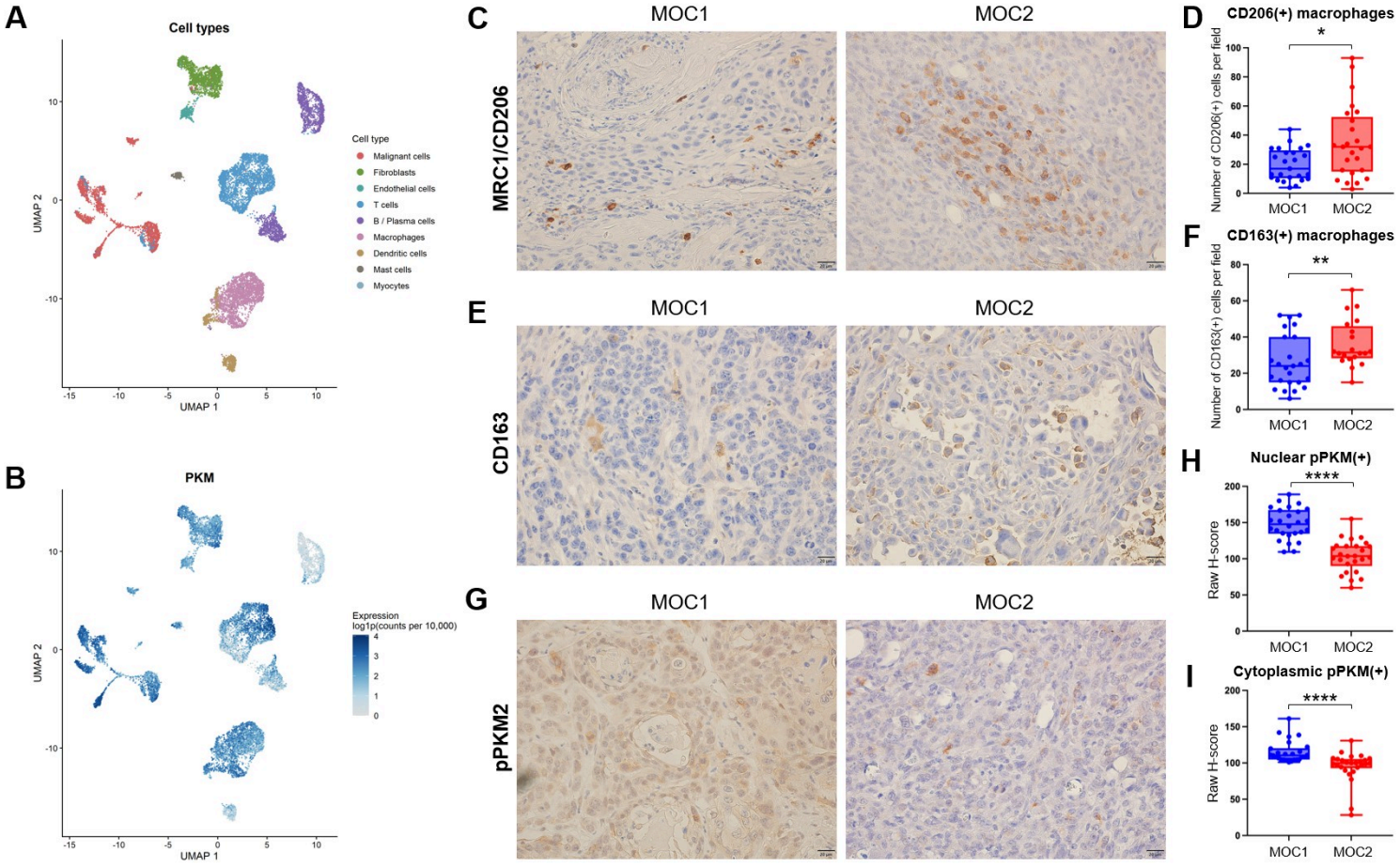


Figure 7

Expression of total PKM and phosphorylated PKM2 (pPKM2) in oral carcinomas. (A, B) Single-cell RNA-seq analysis of oral carcinoma. N=13. Cell types (A) and PKM expression (PKM1 + PKM2) (B) were analyzed. (C–I) M1/M2 macrophages and pPKM2 in immunogenic (MOC1) and immunosuppressive (MOC2) orthotopic oral carcinoma models. (C, E, G) Representative IHC images of M2-type macrophage markers, MRC1/CD206 (C) and CD163 (E), as well as phosphorylated PKM2 (G). Scale bars: 20 μm. (D, F,

H, I) Box-and-whisker plots comparing CD206-positive cells (D), CD163-positive cells (F), nuclear pPKM2 (H), and cytoplasmic pPKM2 (I) in the MOC1/2 models. Statistical significance was assessed using the Mann-Whitney U (Wilcoxon rank-sum) test, unpaired, two-tailed. n = 26, *p < 0.05, **p < 0.01, ****p < 0.0001.

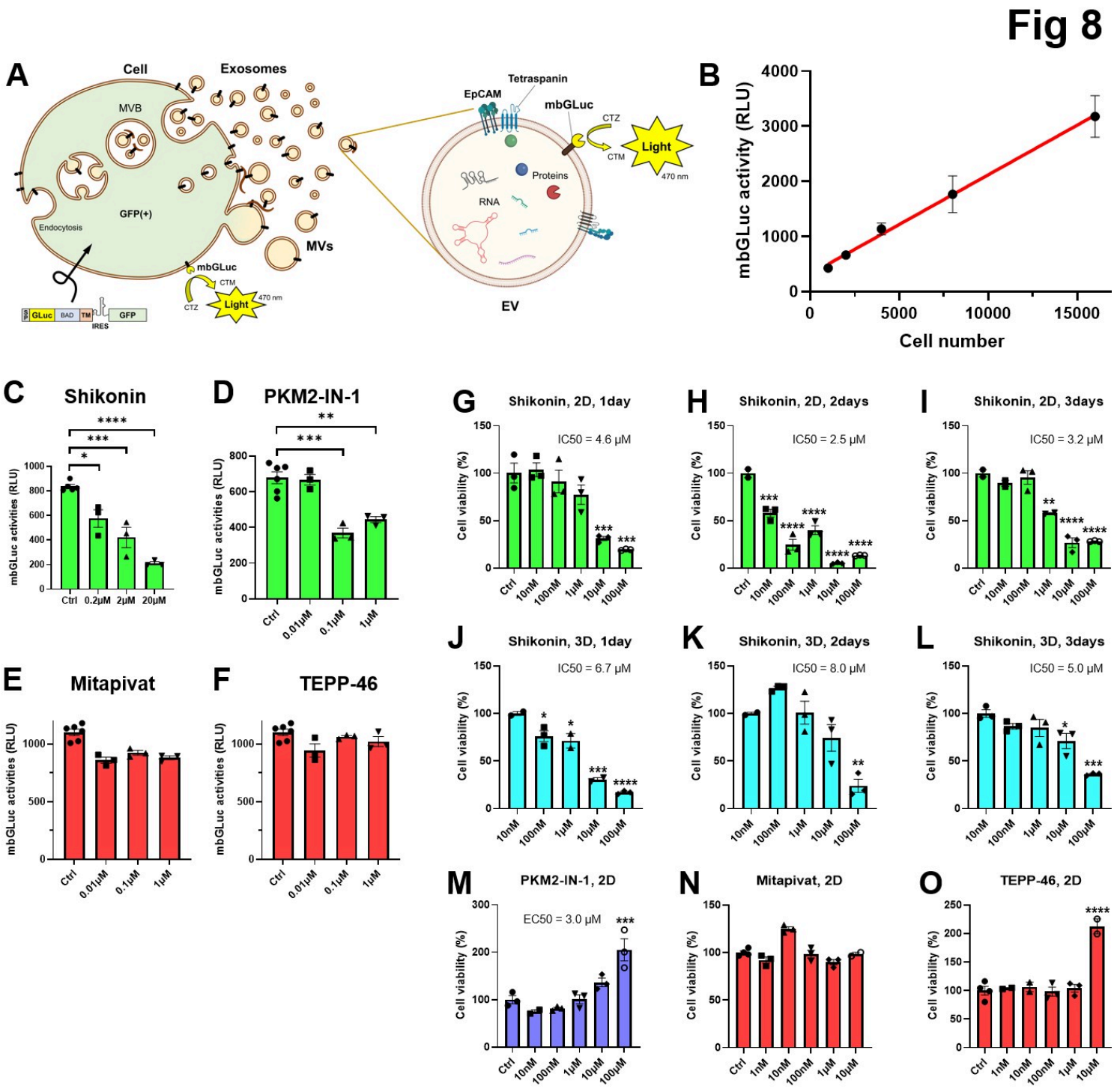


Figure 8

PKM2 activity regulates EV secretion and viability in oral cancer cells. (A) Schematic of the membrane-bound Gaussia luciferase (mbGluc) reporter system used to quantify EV secretion in culture

supernatants of M3/mbGluc cells. Illustrations were created using BioRender. (B) Pilot analysis showing a positive correlation between mbGluc activity and cell number. (C,D) Effects of the PKM2 inhibitor shikonin (C) and PKM2-IN-1 (D) on EV secretion (E). (E,F) Effects of the PKM2 activator mitapivat (E) and TEPP-46 (F) on EV secretion. (G–O) Viability of M3 cells**.** M3 cells were treated with PKM2 inhibitors (shikonin or PKM2-IN-1) or activators (mitapivat or TEPP-46) in 2D or 3D cultures. (G–I) Shikonin treatment in 2D culture. (J–L) Effects of shikonin in 3D tumoroid cultures. (M–O) Treatment with PKM-IN-1 (M), mitapivat (N), and TEPP-46 (O) in 2D cultures. Data are presented as mean ± s.e.m. Statistical significance was determined using a one-way ANOVA with Tukey's multiple comparison test; *$p < 0.05$, **$p < 0.01$, ***$p < 0.001$, ****$p < 0.0001$ (n = 3–6 independent cultures).

Supplementary Files

This is a list of supplementary files associated with this preprint. Click to download.

- pkmsupplenoTCnoPageIJOS.docx
- GA.jpg